MYELOID CELLS

Plasma membrane abundance dictates phagocytic capacity and functional cross-talk in myeloid cells

Benjamin Y. Winer^{1,2,3,4}*, Alexander H. Settle¹, Alexandrina M. Yakimov¹, Carlos Jeronimo¹, Tomi Lazarov¹, Murray Tipping⁵, Michelle Saoi⁶, Anjelique Sawh⁷, Anna-Liisa L. Sepp⁸, Michael Galiano⁵, Justin S. A. Perry¹, Yung Yu Wong¹, Frederic Geissmann¹, Justin Cross⁶, Ting Zhou^{9,10}, Lance C. Kam⁸, H. Amalia Pasolli¹¹, Tobias Hohl¹², Jason G. Cyster^{2,13}*, Orion D. Weiner^{3,4}*, Morgan Huse¹*

Professional phagocytes like neutrophils and macrophages tightly control what they consume, how much they consume, and when they move after cargo uptake. We show that plasma membrane abundance is a key arbiter of these cellular behaviors. Neutrophils and macrophages lacking the G protein subunit $G\beta_4$ exhibited profound plasma membrane expansion, accompanied by marked reduction in plasma membrane tension. These biophysical changes promoted the phagocytosis of bacteria, fungus, apoptotic corpses, and cancer cells. We also found that $G\beta_4$ -deficient neutrophils are defective in the normal inhibition of migration following cargo uptake. Sphingolipid synthesis played a central role in these phenotypes by driving plasma membrane accumulation in cells lacking $G\beta_4$. In $G\beta_4$ knockout mice, neutrophils not only exhibited enhanced phagocytosis of inhaled fungal conidia in the lung but also increased trafficking of engulfed pathogens to other organs. Together, these results reveal an unexpected, biophysical control mechanism central to myeloid functional decision-making.



Copyright © 2024 The Authors, some rights reserved; exclusive licensee American Association for the Advancement of Science. No claim to original U.S.

Government Works

INTRODUCTION

Professional phagocytes of the myeloid lineage, including neutrophils and macrophages, maintain homeostasis by clearing apoptotic corpses, cellular debris, and invading pathogens (1–4). Phagocytes take up cargo via phagocytosis, an evolutionarily conserved engulfment process by which cells surround objects and then internalize them. The importance of phagocytosis for proper multicellular physiology is highlighted by the consequences of its dysregulation: Insufficient levels of phagocytic activity increase susceptibility to infection and aging, whereas both excessive and inadequate levels have been linked to autoimmunity, neurodegeneration, and atherosclerosis (5–9). Understanding the molecular pathways and cellular components that control phagocytosis will be critical for mitigating these conditions and also for harnessing professional phagocytes as immunotherapeutic agents to combat infections, cardiovascular disease, and cancer (10–13).

Phagocytosis is triggered by the recognition of cognate cargo ligands, such as phosphatidylserine, complement, and antibodies, by specific receptors on the phagocyte (6). Target recognition elicits

¹Immunology Program, Memorial Sloan Kettering Cancer Center, New York, NY, USA. ²Department of Microbiology and Immunology, University of California San Francisco, San Francisco, CA, USA. ³Cardiovascular Research Institute, University of California San Francisco, San Francisco, CA, USA. ⁴Department of Biochemistry and Biophysics, University of California San Francisco, San Francisco, CA, USA. ⁵Molecular Cytology Core Facility, Memorial Sloan Kettering Cancer Center, New York, NY, USA. ⁶Donald B. and Catherine C. Marron Cancer Metabolism Center, Memorial Sloan Kettering Cancer Center, New York, NY, USA. ⁷New York Structural Biology Center, New York, NY, USA. ⁸Department of Biomedical Engineering, Columbia University, New York, NY, USA. ⁹Center for Stem Cell Biology, Memorial Sloan Kettering Cancer Center, New York, NY, USA. ¹⁰SKI Stem Cell Research Facility, Center for Stem Cell Biology and Developmental Biology Program, Sloan Kettering Institute, 1275 York Avenue, New York, NY, USA. ¹¹Electron Microscopy Resource Center, Rockefeller University, New York, NY, USA. ¹²Human Oncology and Pathogenesis Program, Memorial Sloan Kettering Cancer Center, New York, NY, USA. ¹³Howard Hughes Medical Institute, Chevy Chase, MD, USA.

*Corresponding author. Email: winerb@mskcc.org (B.Y.W.); husem@mskcc.org (M.H.); jason.cyster@ucsf.edu (J.G.C.); orion.weiner@ucsf.edu (O.D.W.)

marked remodeling of the cytoskeleton, which shapes the overlying plasma membrane into a phagocytic cup that embraces and then internalizes the cargo (14, 15). In carrying out their clearance function, myeloid phagocytes exhibit not only robust cargo uptake but also the ability to coordinate this activity with other cellular behaviors (16-20). Cross-talk between phagocytosis and cell motility is particularly well established, with studies documenting an antagonistic relationship between cell migration and engulfment responses in multiple cell types (16-18). In neutrophils specifically, transient arrest after phagocytosis is thought to curtail the dissemination of intracellular microbes (21-23). Accordingly, efforts to modulate the activity of professional phagocytes will require a mechanistic understanding of not only phagocytosis itself but also its regulatory effects on other activities.

Most prior research on phagocytosis has focused on the biochemical mechanisms that control it, and as a result, much is now known about the molecules that mediate cargo recognition and the signal transduction pathways that drive cargo engulfment (24). Phagocytosis is also an intensely physical process (14, 25), implying that it might be subject to biophysical and biochemical modes of regulation. In that regard, the deformability of both cargo and underlying substrate has been shown to modulate the engulfment behavior of macrophages (26-31). However, whether the architecture and mechanics of the phagocyte itself might also influence cargo uptake is not known, and how cell-intrinsic properties of this kind might affect functional cross-talk between phagocytosis and other cellular behaviors is completely unexplored.

The plasma membrane is a particularly interesting candidate mechanoregulator because it must be stretched to build a phagocytic cup and to accommodate increased cellular volume after engulfment (14). Prior work indicates that phagocytosis is both constrained by membrane tension and enhanced by the exocytosis of endomembranes (32–34), implying that the amount of plasma membrane available to a cell might establish its phagocytic capacity. In the present study, we demonstrate that loss of a specific heterotrimeric guanine

nucleotide–binding protein (G protein) subunit, $G\beta_4$, strongly increases the plasma membrane abundance of myeloid cells, leading to enhanced phagocytosis and impaired cross-regulation between phagocytosis and migration. This cellular phenotype markedly alters neutrophil function in vivo, not only driving enhanced consumption of microbes but also increasing trafficking away from the site of infection after pathogen uptake. Hence, the functional potential of immune cells is dictated by their biophysical properties and architectural constraints.

RESULTS

$Geta_4$ deficiency enhances phagocytic responses against a wide range of targets

Heterotrimeric G proteins regulate phagocytosis and migration in multiple myeloid cell types by transducing signals from seventransmembrane G protein-coupled receptors (GPCRs) (35-42). GPCR activation induces dissociation of the G protein α subunit $(G\alpha)$ from the $\beta\gamma$ subcomplex $(G\beta\gamma)$, freeing both components to bind and activate specific downstream effector molecules (43). Most prior research in this area has focused on $G\alpha$ isoforms, whereas comparatively less is known about specific G β and G γ subunits (44). Accordingly, we applied CRISPR-Cas9 to knock out each Gβ subunit in human neutrophil-like HL-60 cells (Fig. 1A and fig. S1, A and B). Gene targeting was carried out in self-renewing HL-60 precursors, which were subsequently differentiated into neutrophillike cells (called HL-60 neutrophils hereafter) by the addition of dimethyl sulfoxide (DMSO). All terminally differentiated cells were CD15⁺ CD16⁺ (fig. S1C), indicating that the genetic modifications that we introduced did not prevent HL-60 progenitors from becoming neutrophils. Knockout and control HL-60 neutrophils were then subjected to phagocytosis assays to investigate potential effects on phagocytosis. As cargo for these experiments, we prepared 10-µm-diameter immunoglobulin G (IgG)-coated polyacrylamide microparticles (MPs) (45, 46) derivatized with two fluorescent dyes: fluorescein isothiocyanate (FITC) and lissamine rhodamine B (LRB; Fig. 1A and fig. S2). FITC, but not LRB, fluorescence is quenched in acidic phagolysosomes, leading to an emission ratio change that can be monitored by flow cytometry and fluorescence microscopy. In this manner, we identified $G\beta$ subunits that either positively or negatively regulated phagocytosis. Consistent with prior work (38, 39), HL-60 neutrophils lacking Gβ₂ exhibited a ~50% reduction in particle uptake (Fig. 1B). By contrast, depletion of $G\beta_4$ induced a notable three- to fourfold increase in phagocytosis relative to wild-type (WT) controls (Fig. 1B). This hyperphagic behavior resulted directly from loss of G β_4 , because reexpression of G β_4 on the knockout background restored phagocytosis to WT levels (Fig. 1C and fig. S3A). The G β_4 knockout (Δ G β_4) phenotype was also cell intrinsic, because it was readily apparent in both monocultures and cocultures containing a 1:1 mixture of WT and $\Delta G\beta_4$ HL-60 neutrophils (Fig. 1D). Phagosome acidification, which we measured using MPs conjugated to pH-sensitive pHrodo dyes, was unaffected by $G\beta_4$ deficiency (fig. S3B), strongly suggesting that the hyperphagia that we observed reflected increased uptake rather than accelerated phagosome maturation.

 $G\beta_4$ deficiency markedly enhanced particle consumption on a percell basis. In wide-field imaging experiments, almost half of the phagocytic $\Delta G\beta_4$ cells engulfed two or more MPs, whereas the vast majority of phagocytic WT cells took up just one (Fig. 1E). Superresolution microscopy of individual phagocytic events revealed

intriguing differences in engulfment dynamics. $\Delta G\beta_4$ HL-60 neutrophils formed stereotypical phagocytic cups featuring a pronounced band of filamentous actin (F-actin) at the leading edge (Fig. 1F). This morphology was much less apparent in WT cells, which still engaged MP targets but only achieved full engulfment in less than 50% of conjugates. In contrast, $\Delta G\beta_4$ HL-60 neutrophils completed over 90% of their phagocytic attempts and executed engulfment more than twice as fast as their WT counterparts (Fig. 1G and movie S1). To investigate whether this enhanced rate of phagocytosis reflected higher levels of environmental probing, we calculated the "ruffling index" of both $\Delta G\beta_4$ and WT HL-60 neutrophils from live videos of fluorescently labeled cells (47, 48). $\Delta G\beta_4$ cells exhibited a twofold increase in this ruffling index (Fig. 1H), indicative of increased physical activity and consistent with their enhanced phagocytic potential.

To further explore the scope of the $\Delta G\beta_4$ phenotype, we challenged WT and $\Delta G\beta_4$ HL-60 cells with MPs bearing alternative coatings, including phosphatidylserine (PS), complement, IgG, and IgA. $\Delta G\beta_4$ cells phagocytosed 2- to 10-fold more cargo in each case, indicating that their hyperphagia was not limited to a specific uptake receptor (fig. S3C). Next, we measured the phagocytosis of four distinct biological targets: the Gram-negative bacterium *Pseudomonas* aeruginosa, Staphylococcus aureus bioparticles, conidia from the fungus Aspergillus fumigatus, and apoptotic Jurkat T cell corpses (Fig. 2A and fig. S3, D and E). These experiments used both HL-60 neutrophils and HL-60-derived macrophages (HL-60 macrophages), which we differentiated from progenitors using 12-Otetradecanoylphorbol-13-acetate (49, 50). ΔGβ4 cells outperformed WT controls in every case, further supporting the hypothesis that Gβ₄ deficiency potentiates phagocytosis against diverse biological cargos. We also examined macropinocytosis, an F-actin-dependent process used by professional phagocytes to ingest antigen and other soluble factors (51). Although a similar fraction of WT and Δ G β 4 HL-60 neutrophils performed macropinocytosis, which we quantified by uptake of fluorescent 70-kDa dextran, ΔGβ4 cells took up substantially more cargo per cell (Fig. 2B). Hence, Gβ4 deficiency affects multiple cargo uptake mechanisms.

Next, we investigated whether loss of $G\beta_4$ could augment the therapeutic phagocytosis of tumors. Cancer cells may evade immune detection and clearance by expressing CD47, a cell surface protein that has been proposed to function as a "don't eat me" signal (52, 53). Antibodies or peptides against CD47 or its receptor, signal regulatory protein α (SIRP α), can stimulate an engulfment response either by blocking the "don't eat me signal" or by opsonizing the cancer cell for phagocytosis (54-58). To adapt this approach to our experimental system, we challenged HL-60 neutrophils with Ramos B lymphoma target cells in the absence or presence of anti-CD47 blockade. Antibodies against the B cell marker CD20 were added to further promote phagocytosis via Fc receptor engagement. WT HL-60 neutrophils did not take up Ramos cells, and treatment with anti-CD47 and/or anti-CD20 failed to enhance their activity. In contrast, ΔGβ₄ HL-60 neutrophils exhibited a low but measurable level of baseline phagocytosis, which increased threefold in the presence of anti-CD47 and even more so (eightfold) when anti-CD47 was combined with anti-CD20 (Fig. 2C). These results suggest that Gβ₄ deficiency augments weak phagocytic responses against tumor cells.

Phosphoinositide 3-kinases (PI3Ks) promote phagocytosis, particularly the uptake of large cargos, by generating phosphatidylinositol 3,4,5-trisphosphate (PIP₃) at the phagocytic cup (59, 60). The hyperphagic behavior of $\Delta G\beta_4$ cells raised the possibility that they

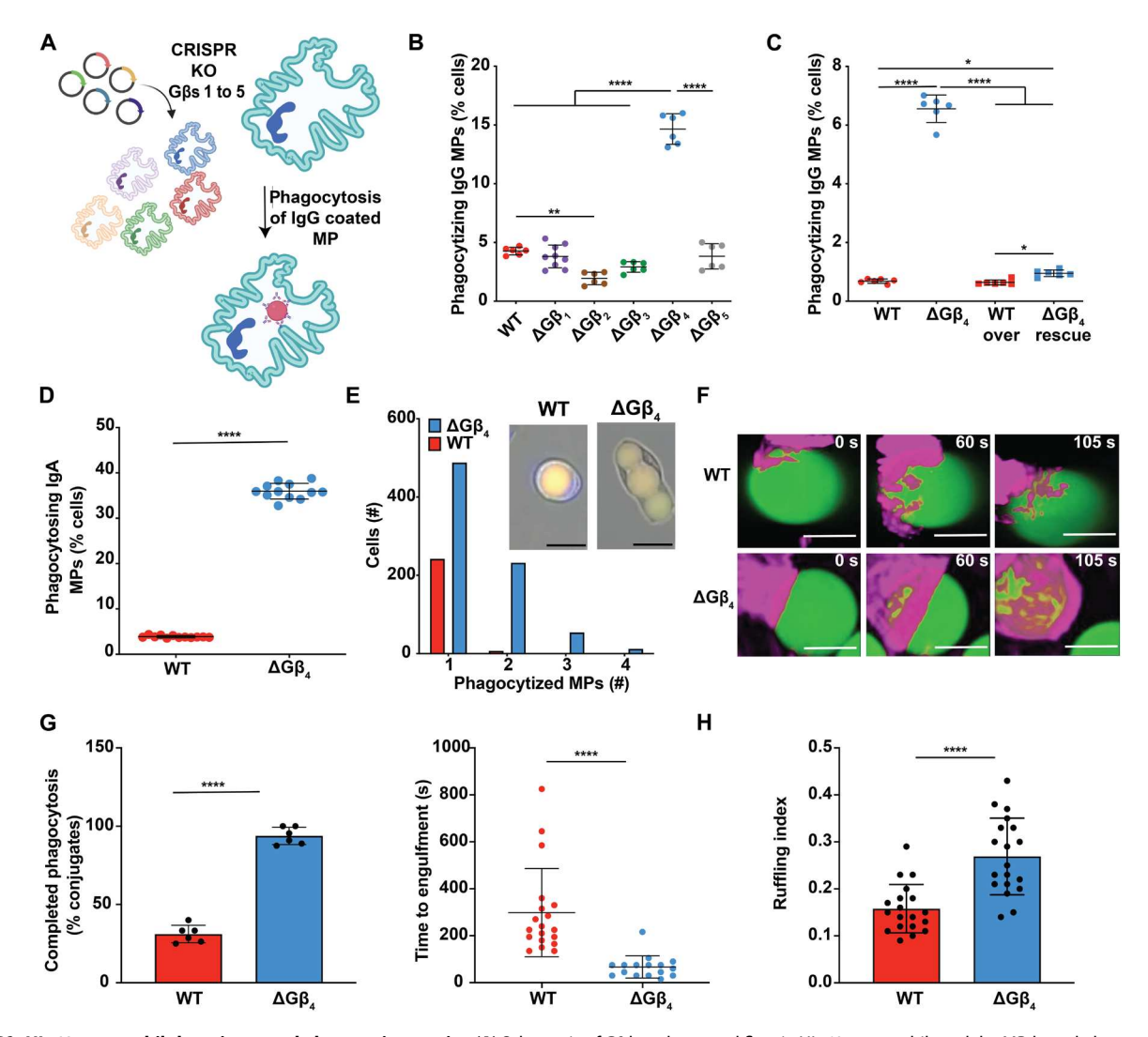


Fig. 1. Δ **Gβ**₄ **HL-60** neutrophils have increased phagocytic capacity. (**A**) Schematic of Gβ knockout workflow in HL-60 neutrophils and the MP-based phagocytosis assay. (**B**) WT and Δ Gβ HL-60 neutrophils were challenged with human IgG-coated MPs and phagocytosis quantified after 3 hours. Data are means \pm SD. (**C**) WT and Δ Gβ₄ HL-60 neutrophils transfected with exogenous Gβ₄ (WT over and Δ Gβ₄ rescue) or control lentivirus (WT and Δ Gβ₄) were challenged with human IgG-coated MPs and phagocytosis quantified after 3 hours. Data are means \pm SD. For (B) and (C), $n \ge 6$ for each sample, pooled from three biological replicates. One-way ANOVA with Tukey's multiple comparisons test, *P < 0.05, **P < 0.01, and ****P < 0.0001. (**D**) Δ Gβ₄ and WT HL-60 neutrophils were stained with different fluorophores, mixed 1:1, and then challenged with IgA-coated MPs. The graph shows phagocytic uptake after 3 hours. Data are means \pm SD. n = 12 for each sample, pooled from three biological replicates. Unpaired t test, *****P < 0.0001. (**E**) Δ Gβ₄ and WT HL-60 neutrophils were challenged with IgA-coated MPs and imaged over 3 hours to assess per-cell phagocytic capacity. The histogram shows the number of Δ Gβ₄ and WT cells that consumed one, two, three, or four MPs during the experiment. Data were pooled from five biological replicates. The inset shows sample images of WT and Δ Gβ₄ cells after MP uptake. Scale bars, 20 μm. (**F** and **G**) WT and Δ Gβ₄ HL-60 neutrophils expressing F-tractin-mCherry (magenta) were fed IgG-coated MPs (green), and phagocytic uptake was monitored for 10 to 30 min. (**F**) Representative interactions are shown in time-lapse montage format. Scale bars, 5 μm. (G) Quantification of the frequency (left) and speed (right) of phagocytosis. Data points in the left graph correspond to mean values in each movie, whereas data points in the right graph denote individual cells. Bars denote means \pm SD, pooled from six biological replicates. Unpaired t test, ****P <

might have enhanced or otherwise modulated PI3K activity. During phagocytosis of IgG-coated MPs, however, WT and $\Delta G\beta_4$ HL-60 neutrophils exhibited similar levels of PIP₃ enrichment at the phagocytic cup, which we measured using a PIP₃ biosensor containing the AKT pleckstrin homology domain linked to blue fluorescent protein (PH-AKT-BFP) (fig. S4, A and B). Furthermore, the inhibition of PI3K activity using the small molecule PIK90 abrogated MP uptake in both cell types (fig. S4C). Thus, $G\beta_4$ deficiency neither

enhances nor circumvents the need for PI3K signaling during phagocytosis.

$G\beta_4$ deficiency alters cell migration and cross-talk between phagocytosis and motility

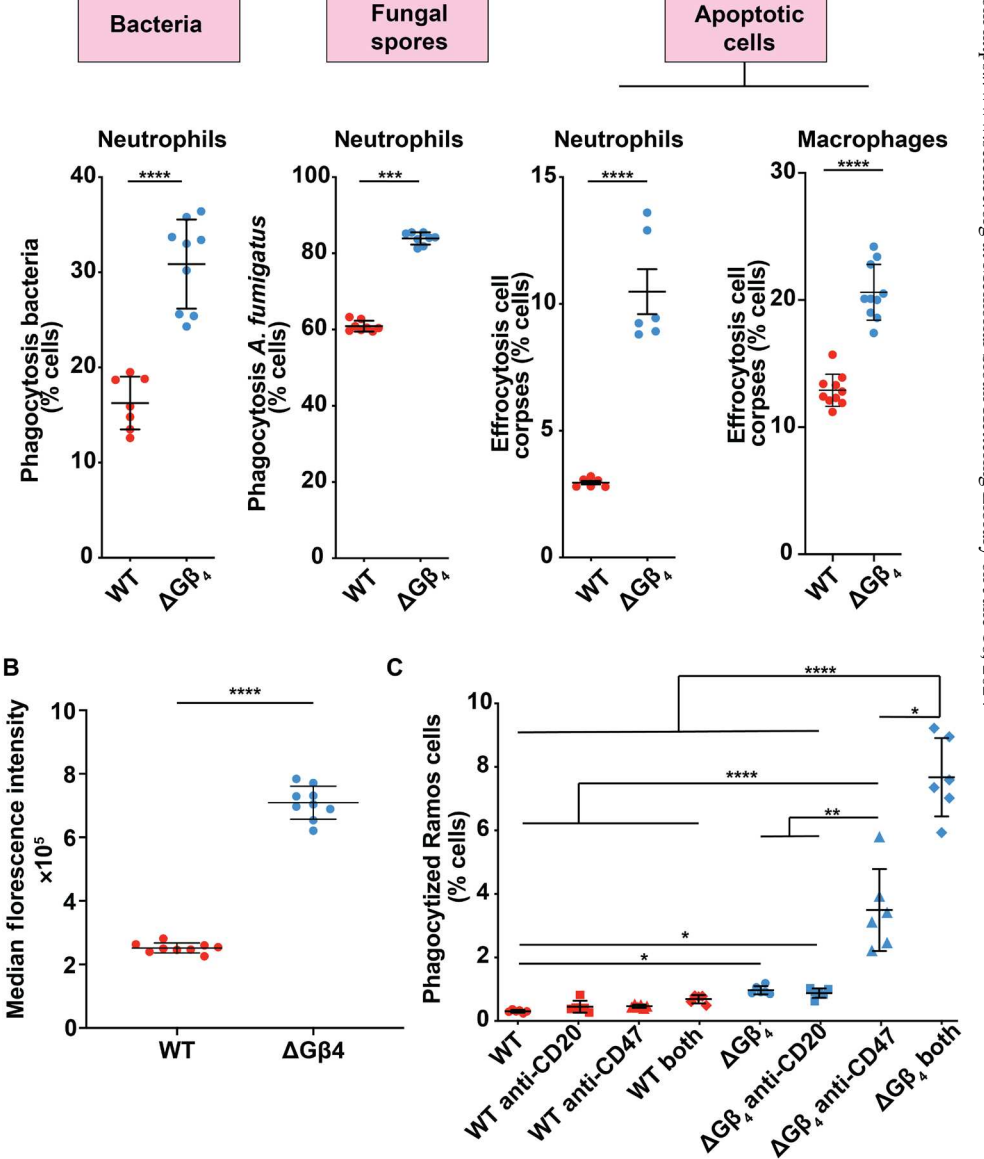
Because proper coordination between cargo uptake and motility is essential for myeloid cell function (16-18), we next investigated the effects of G β_4 on cell migration. To this end, we used a chemotaxis

assay in which HL-60 neutrophils were attached to fibronectincoated glass and then presented with a point source of the peptide chemoattractant fMLF (N-formyl-methionyl-leucyl-phenylalanine), applied via micropipette (Fig. 3A). Under these conditions, neutrophils adopt a fan-like morphology with a broad leading edge directed toward the point source and a thin uropod trailing behind. Both $\Delta G\beta_4$ and WT cells were able to migrate up the fMLF gradient and moved at similar velocities during the first 15 min of each experiment (Fig. 3B). Δ G β 4 cells slowed substantially over the remainder of the experiment, however, leading to a reduction in mean velocity over the entire 1-hour time course (Fig. 3C and movie S2). This reduced motility was associated with the formation of extended "tails" at the rear of migrating $\Delta G\beta_4$ cells, suggestive of a defect in uropod retraction (Fig. 3D). We observed multiple instances in which elongated $\Delta G\beta_4$ cells appeared to be "struggling" against their own uropod to make forward progress (Fig. 3D). We obtained a similar set of results using HL-60 macrophages. In a uniform

chemokinetic field of fMLF, $\Delta G\beta_4$ HL-60 macrophages moved slower than their WT counterparts and also formed elongated uropods during migration (fig. S5, A to C). In some cases, $\Delta G\beta_4$ macrophages exhibited multiple extended tails (fig. S5D), implying a defect in cell polarity. Collectively, these results indicate that $G\beta_4$ deficiency impairs motility and alters migratory cell morphology in myeloid cells.

Next, we interrogated cross-talk between phagocytosis and migration by quantifying the motility of HL-60 neutrophils after uptake of one IgG-coated MP. WT and $\Delta G\beta_4$ cells were exposed to MPs with distinct fluorescent labels [pHrodo Red (WT) versus pHrodo Green ($\Delta G\beta_4$)] to facilitate imaging and tracking in mixed samples. MP consumption slowed the movement of WT HL-60 neutrophils considerably relative to MP-less WT controls (Fig. 3C). By contrast, $\Delta G\beta 4$ cells containing MPs moved at the same rate as their MP-less $\Delta G\beta 4$ counterparts (Fig. 3C). Although the instantaneous speed of MP-bearing $\Delta G\beta 4$ neutrophils remained slightly less

Fig. 2. $\Delta G \beta_4$ hyperphagia applies to a wide range of biological targets. (A) $\Delta G\beta_4$ and WT HL-60 neutrophils or macrophages were challenged with fluorescently labeled P. aeruginosa (left), A. fumigatus (middle), or apoptotic Jurkat cell corpses (right), and phagocytosis was quantified after 3 hours. Data are means \pm SD. $n \ge 7$ for each sample, pooled from three biological replicates. Unpaired t test, ***P < 0.001 and ****P < 0.0001. (**B**) Δ G β ₄ and WT HL-60 neutrophils were incubated with fluorescent 70-kDa dextran to measure macropinocytosis. The graph shows the quantification of engulfed dextran. Data are means + SD. n > 9 for each sample, pooled from three biological replicates. Unpaired t test, ****P < 0.0001. (**C**) Δ G β_4 and WT HL-60 neutrophils were challenged with RAMOS B lymphoma cells in the presence or absence of anti-CD20 and anti-CD47. Data are means \pm SD. $n \ge 5$ for each sample, pooled from three biological replicates. Two-way ANOVA with Šidák's multiple comparisons test, *P < 0.05, **P < 0.01, and ****P < 0.0001.



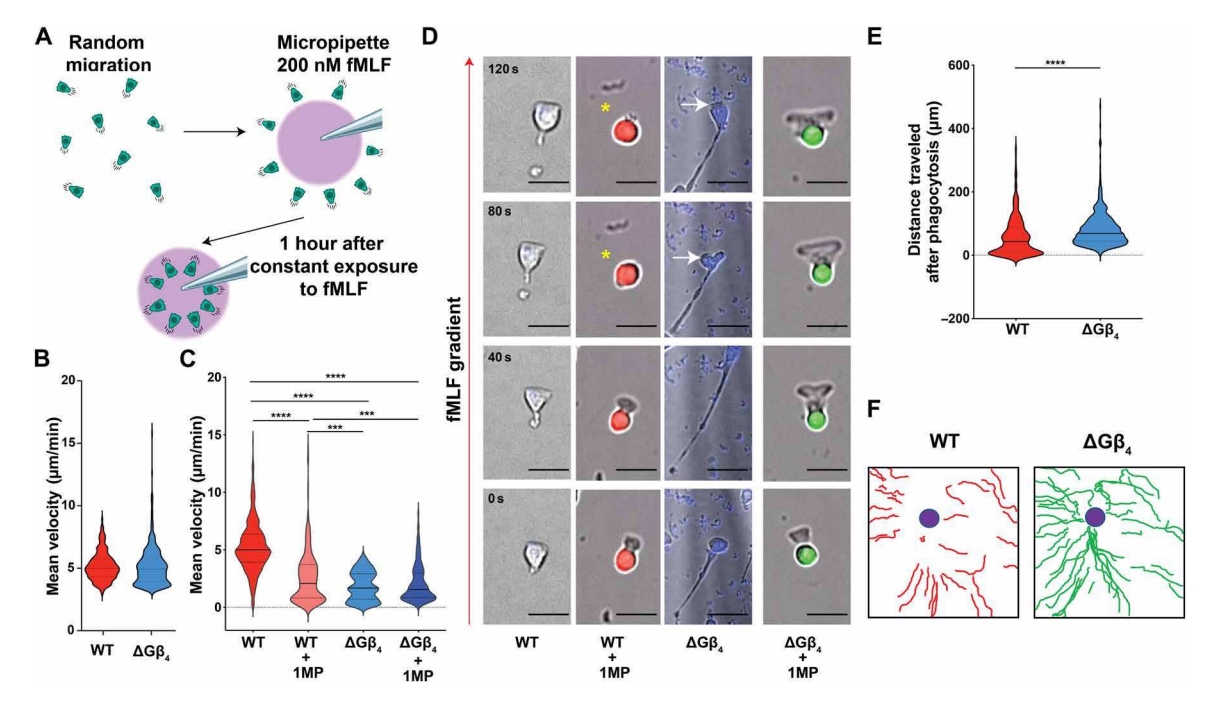


Fig. 3. GB_4 deficiency alters cell migration and cross-talk between phagocytosis and motility. (A) Schematic of the micropipette-based chemotaxis assay. (B to F) ΔGB_4 and WT HL-60 neutrophils were seeded onto fibronectin-coated slides and exposed to 200 nM fMLF delivered through a micropipette over the course of an hour. Alternatively, ΔGB_4 and WT cells that had consumed one MP (WT + 1MP and ΔGB_4 + 1MP) were sorted, seeded at a 1:1 ratio on fibronectin-coated glass, and exposed to 200 nM fMLF through a micropipette for 1 hour. (B) Mean velocity of ΔGB_4 and WT HL-60 neutrophils during the first 15 min of the time course. (C) Mean velocities of WT, WT + 1MP, ΔGB_4 , and ΔGB_4 + 1MP cells were calculated from three separate 1-hour videos. (D) Time-lapse montages of representative cells in each experimental group, with the red arrow indicating the direction of the fMLF gradient. Yellow asterisks denote a transient loss of migratory cell polarity in a WT + 1MP cell. White arrows indicate cell body regression in a ΔGB_4 cell with an extended uropod. Scale bars, 20 µm. (E) Total distance travelled by WT + 1MP and ΔGB_4 + 1MP cells after 1 hour of exposure to 200 nM fMLF. (F) Representative migration tracks for WT + 1MP and ΔGB_4 + 1MP over the course of 1-hour exposure to 200 nM fMLF. Violins in (B, C, and E) encompass the entire distribution, with solid horizontal lines indicating the median and dotted lines indicating the upper and lower quartiles. ***P < 0.001 and ****P < 0.0001, calculated by unpaired t test (E) or two-way ANOVA with Šidák's multiple comparisons test (C). $n \ge 174$ for each sample, pooled from three biological replicates.

than that of MP-bearing WT cells, their migration was more persistent, yielding substantially longer tracks that more closely approached the fMLF point source (Fig. 3, E and F, and movie S2). These motility phenotypes were mirrored by changes in cell shape. In WT HL-60 neutrophils, phagocytosis appeared to hamper migratory polarization; cells periodically collapsed into a rounded configuration, and these morphological changes tended to coincide with stalls in motility (Fig. 3D and movie S2). By contrast, $\Delta G\beta_4$ morphology was normalized by MP uptake; MP-bearing cells formed persistent leading edges and lacked the extended uropods characteristic of the cargoless state (Fig. 3D). Hence, $G\beta_4$ depletion affects neutrophil migration in two ways: It reduces the speed of unencumbered cells, and it also impairs inhibitory cross-regulation between phagocytosis and motility.

$G\beta_4$ deficiency alters lipid composition and plasma membrane abundance

The notable uropod extension displayed by migrating $\Delta G\beta_4$ HL-60 cells was suggestive of a substantial change in cellular architecture. Consistent with this notion, scanning electron microscopy (SEM) indicated that $\Delta G\beta_4$ HL-60 cells had a more ruffled surface appearance than WT controls (Fig. 4A). To investigate this structural difference more closely, we performed focused ion beam (FIB)–SEM, a method in which successive sections from the same sample are imaged by SEM and then used to generate a nanometer-resolution

three-dimensional (3D) reconstruction (61). WT and $\Delta G\beta_4$ HL-60 cells were osmium-stained to highlight lipid-rich cellular components, embedded in resin, and subjected to FIB-SEM at 40-nm sectioning. Supervised machine learning was used to define the plasma membrane in each image, followed by 3D rendering (62). The resulting reconstructions revealed notable differences in plasma membrane configuration. Whereas the surface of WT cells was mostly smooth with small extensions, $\Delta G\beta_4$ cells exhibited large flaps of plasma membrane projecting up to 10 µm from the cell body (Fig. 4B and movie S3). The presence of these structures increased the surface-to-volume ratio of $\Delta G\beta_4$ HL-60 neutrophils by a factor of two relative to WT controls (Fig. 4C). $\Delta G\beta_4$ cells also contained larger and more numerous cytoplasmic lipid droplets, which appeared as high-contrast compartments in osmium-stained FIB-SEM images (Fig. 4, B, D, and E). Using FM64 and BODIPY staining, we confirmed that loss of Gβ₄ leads to excess accumulation of plasma membrane and lipid droplets, respectively (fig. S6, A to C). Together, these data indicate that $G\beta_4$ controls membrane architecture and lipid content in neutrophils.

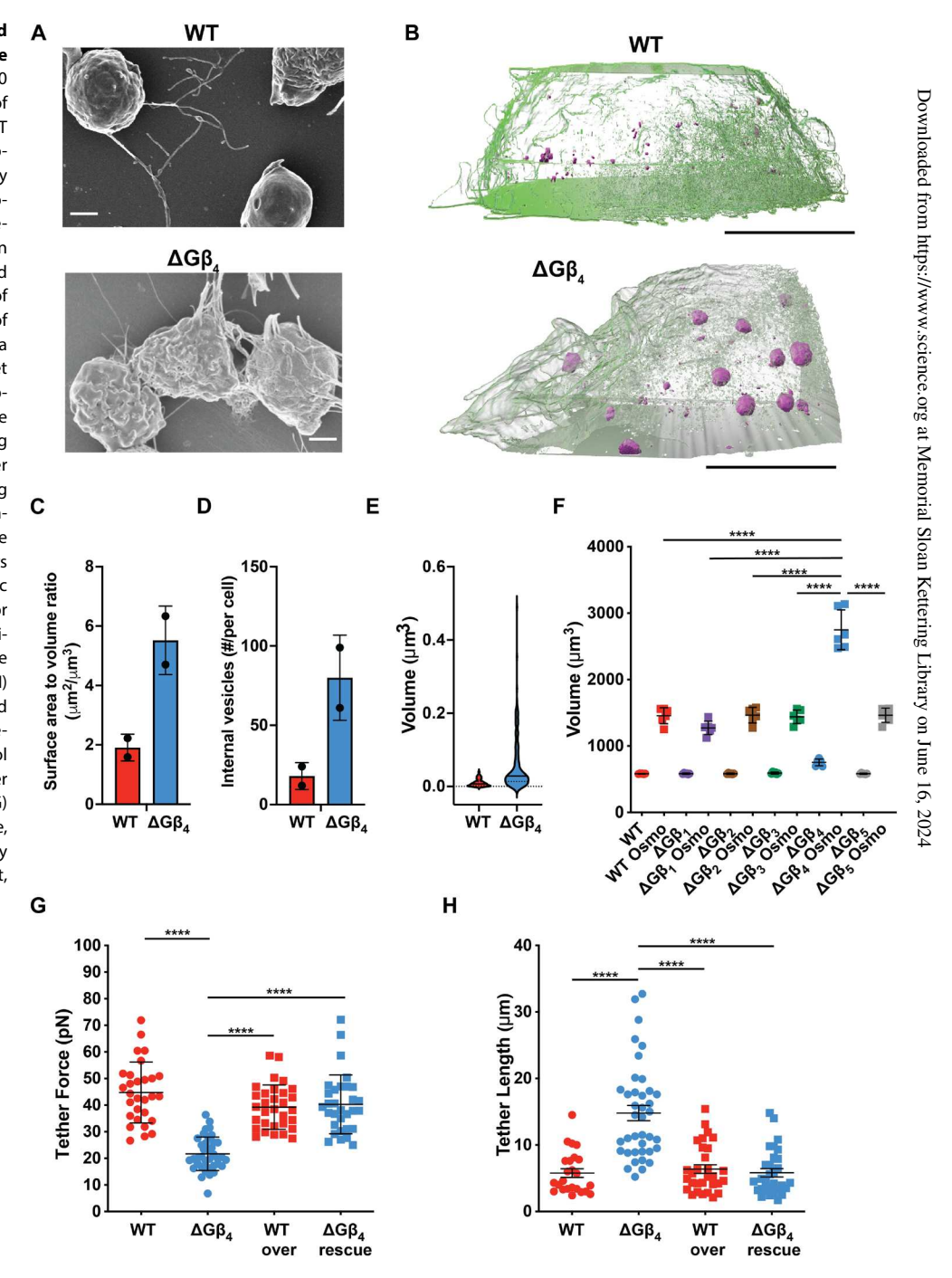
We considered the possibility that excess plasma membrane might concomitantly increase surface expression of Fc receptors and thereby enhance phagocytosis. $\Delta G\beta_4$ and WT HL-60 neutrophils, however, expressed similar levels of Fc γ RII and Fc γ RII and little to no Fc γ RIII (fig. S7, A to C), arguing against a role for Fc receptor overexpression in the $\Delta G\beta_4$ hyperphagic phenotype. SIRP α levels

were similarly unaffected by $G\beta_4$ deficiency (fig. S7D). $\Delta G\beta_4$ and WT HL-60 neutrophils also contained nearly equivalent levels of F-actin, which we visualized by phalloidin staining, and most cells of either genotype exhibited canonical migratory cell morphology, defined by strong F-actin accumulation at the leading edge (fig. S7, E and F). Hence, excess plasma membrane did not appear to cause cytoskeletal dysregulation in $\Delta G\beta_4$ cells.

Having ruled out these potential mechanisms, we turned our attention to the biophysical and functional effects of $G\beta_4$ deficiency on the plasma membrane itself. Acute osmotic shock swells cells to

the limits of their plasma membrane capacity, thereby enabling comparisons of total surface area. $\Delta G\beta_4$ HL-60 neutrophils were only slightly larger than their WT counterparts under isotonic conditions. Upon transfer to hypotonic medium, however, $\Delta G\beta_4$ cells expanded to twice the size of controls (Fig. 4F). Assuming that swelled HL-60 neutrophils are spherical, this volume differential implies a ~60% increase in plasma membrane surface area. Excess plasma membrane would be expected to facilitate the formation of phagocytic cups and thereby promote engulfment. To quantify membrane mobilization during cup formation, we used a "frustrated

Fig. 4. $\Delta G \beta_4$ HL-60 neutrophils have increased plasma membrane and decreased membrane tension. (A) SEM images of WT and $\Delta G\beta_4$ HL-60 neutrophils. Scale bars, 2 µm. Representative of five biological replicates. (**B** to **E**) $\Delta G\beta_4$ and WT HL-60 neutrophils stained with potassium ferrocyanide and osmium tetroxide were imaged by FIB-SEM (n = 2 of each cell type, from one biological replicate). (B) 3D reconstructions of representative cells, with plasma membrane shown in semitransparent green and lipid droplets in solid magenta. Scale bars, 5 µm. (C) Quantification of surface area to volume ratio. (D) Quantification of lipid droplet number per cell. In (C) and (D), data are means \pm SD. (E) Quantification of lipid droplet volume (n = 20 droplets in WT cells and 24 droplets in $\Delta G\beta_4$ cells). Violins encompass the entire distribution, with solid horizontal lines indicating the median and dotted lines indicating the upper and lower quartiles. (F) HL-60 neutrophils lacking the indicated G_β subunits, along with WT controls, were subjected to osmotic shock to induce swelling to maximal volume. The graph shows volume measurements before and after osmotic shock (Osmo). Data are means \pm SEM. n=6 for each sample, pooled from three biological replicates. One-way ANOVA with Tukey's multiple comparisons test, ****P < 0.0001. (**G** and **H**) Membrane tethers were generated from WT and ΔGβ₄ HL-60 neutrophils transduced with exogenous $G\beta_4$ (WT over and $\Delta G\beta_4$ rescue) or control lentivirus (WT and $\Delta G\beta_4$). (G) Membrane tether forces. (H) Membrane tether lengths. Data in (G) and (H) are means \pm SD. $n \ge 29$ for each sample, pooled from five biological replicates. Two-way ANOVA with Šidák's multiple comparisons test, ****P < 0.0001.



phagocytosis" assay (63, 64) in which HL-60 neutrophils were applied to IgG-coated glass slides. Neutrophils and macrophages form flat, unresolved phagocytic cups on surfaces of this kind, which are easily visualized by total internal reflection fluorescence microscopy. Frustrated phagosomes formed by $\Delta G\beta_4$ HL-60 neutrophils were substantially larger than those of WT controls (fig. S8), consistent with a role for increased membrane abundance in phagocytic cup formation.

Membrane tension is known to inhibit both phagocytosis and migration, presumably by mechanically constraining the formation of actin-based structures and/or activating inhibitory mechanosensory pathways (63). We speculated that, by increasing plasma membrane abundance, Gβ₄ deficiency might reduce membrane tension and thereby attenuate these regulatory effects. To explore this possibility, we used an established approach in which a concanavalin A-coated bead is adsorbed to the cell surface and then pulled away using an optical trap (65). The displaced bead remains attached to the cell via a thin membrane tether, which exerts a restoring force that is proportional to the square of membrane tension (66, 67). In this manner, we found that Gβ₄ deficiency reduced tether forces by a factor of two in HL-60 neutrophils (Fig. 4G). Δ G β 4 cells also generated longer tethers then WT controls, indicating that they had larger plasma membrane reservoirs (Fig. 4H) (68). Rescue experiments confirmed that both phenotypes were specific to Gβ4 (Fig. 4, G and H). In conjunction with the imaging and osmotic shock studies described above, these results suggest a central role for plasma membrane abundance in the regulation of neutrophil effector responses.

To explore potential mechanisms underlying the $\Delta G\beta_4$ plasma membrane phenotype, we subjected $\Delta G\beta_4$ and WT HL-60 neutrophils to comparative lipidomics (fig. S9, A and B, and data file S1). As expected, $\Delta G\beta_4$ cells contained more total lipids than WT controls on a per-cell basis (fig. S9C). This increase did not apply equally to all lipid subtypes, however, because many species were unchanged in proportion between samples and some, like hexosylceramides, were more abundant in WT cells (fig. S9D). $\Delta G\beta_4$ cells were distinguished by a disproportionate enrichment of sphingolipids, particularly ceramide and sphingomyelin (Fig. 5A and fig. S9C), which are predominantly found in the plasma membrane. Using RNA sequencing, we observed selective up-regulation of sphingolipid synthesis genes in $\Delta G\beta_4$ neutrophils after MP exposure (Fig. 5B), establishing an additional link between sphingolipids and the $\Delta G\beta_4$ phenotype. To interrogate the role of sphingolipids in plasma membrane expansion more directly, we asked whether the inhibition of sphingolipid synthesis could reverse the effects of Gβ₄ deficiency. To this end, we applied the small molecule myriocin, a potent inhibitor of serine palmitoyltransferase, the first enzyme in the sphingolipid synthesis pathway (fig. S9E) (69, 70). Myriocin treatment during differentiation restored the membrane tension of Δ G β_4 HL-60 cells to WT levels (Fig. 5C), and it also largely reversed their hyperphagic behavior (Fig. 5D), their extended migratory morphology (Fig. 5E), and their motility defect (Fig. 5F). By contrast, acute treatment of fully differentiated $\Delta G\beta_4$ HL-60 cells with myriocin had no effect on MP uptake (fig. S9F), suggesting that the functionally relevant effects of Gβ₄ signaling on sphingolipid synthesis occur during the differentiation phase. Collectively, these results indicate that the excess plasma membrane characteristic of $\Delta G\beta_4$ cells is due, at least in part, to increased sphingolipid synthesis.

$G\beta_4$ controls membrane abundance and phagocytosis in primary myeloid cells

Having demonstrated that Gβ₄ deficiency induces hyperphagia in HL-60 neutrophils and macrophages, we next investigated whether this phenotype would manifest in primary cells. By applying CRISPR-Cas9 targeting to the estrogen-regulated (ER)-HoxB8 immortalized murine progenitor system (fig. S10, A and B) (22, 71, 72), we were able to generate primary-like neutrophils lacking Gβ₄, along with controls expressing nontargeting guide RNA (gRNA). Both ΔGβ4 and WT ER-HoxB8 neutrophils expressed equivalent levels of CD11b and Ly6G after differentiation (fig. S10C), indicating that Gβ₄ is dispensable for the acquisition of neutrophil fate. As with $\Delta G\beta_4$ HL-60 cells, $\Delta G\beta_4$ ER-HoxB8 neutrophils displayed clear signs of plasma membrane dysregulation, including reduced membrane tension and increased membrane tether length in optical trap experiments (fig. S10, D and E). $\Delta G\beta_4$ ER-HoxB8 neutrophils also expanded to nearly twice the volume of WT controls upon transfer to hypotonic medium (fig. S10F). In phagocytosis assays, both WT and $\Delta G\beta_4$ ER-HoxB8 neutrophils failed to consume IgG-coated MPs, likely because primary murine neutrophils are substantially smaller than HL-60 neutrophils and therefore unable to accommodate larger (diameter, ~10 µm) cargos. When challenged with smaller (diameter, 2 µm) S. aureus bioparticles, however, $\Delta G\beta_4$ ER-HoxB8 neutrophils more than doubled the uptake of WT controls (fig. S10G).

To assess the role of $G\beta_4$ signaling in primary macrophages, we prepared WT and ΔGβ₄ macrophages from human induced pluripotent stem cells (hiPSCs; Fig. 6A and fig. S11A) (73-75). CRISPR-Cas9 was used to target the GNB4 locus (encoding G β_4) at the hiPSC stage, and WT control hiPSCs were generated in parallel using a nontargeting gRNA (fig. S11B). Granulocyte monocyte progenitor (GMP) cells derived from these hiPSC lines were then differentiated into mature CD11b⁺ CD14⁺ CD68⁺ macrophages. Gβ₄ deficiency did not affect the efficacy of this differentiation protocol (fig. S11C). In optical trap experiments, $\Delta G\beta_4$ macrophages generated weaker tether forces and longer membrane tethers than WT controls (Fig. 6, B and C). $\Delta G\beta_4$ macrophages also became substantially larger than their WT counterparts in hypotonic medium, despite being similarly sized under isotonic conditions (Fig. 6D). These phenotypes, which mirrored our results in the HL-60 and ER-HoxB8 systems, were strongly suggestive of excess plasma membrane accumulation. Last, we evaluated phagocytic capacity and found that Gβ₄ deficiency markedly increased the uptake of IgG-coated MPs (Fig. 6E). We conclude that the Gβ₄ pathway regulates plasma membrane abundance and phagocytosis in primary neutrophils and macrophages.

Gβ₄ regulates antifungal immunity in vivo

Phagocytes are the first line of defense against microbes in multiple epithelial tissues (3, 13, 76). To evaluate the role of G β_4 -dependent membrane allocation during this early phase of immunity, we generated mice with a targeted deletion of exon 4 of the *Gnb4* locus (fig. S12, A and B). This modification prematurely terminated the *Gnb4* open reading frame, leading to constitutive G β_4 deficiency. Mice homozygous for this deletion ($Gnb4^{-/-}$) and WT ($Gnb4^{+/+}$) littermate controls were infected intratracheally with A. *fumigatus*, a fungal pathogen that elicits the robust recruitment of phagocytically active neutrophils to the lung (77–79). To enable flow cytometric detection of fungal uptake by these cells, we used fluorescent Aspergillus reporter (FLARE) conidia that expressed DsRed, a degradable fluorescent protein, and were also labeled with Alexa

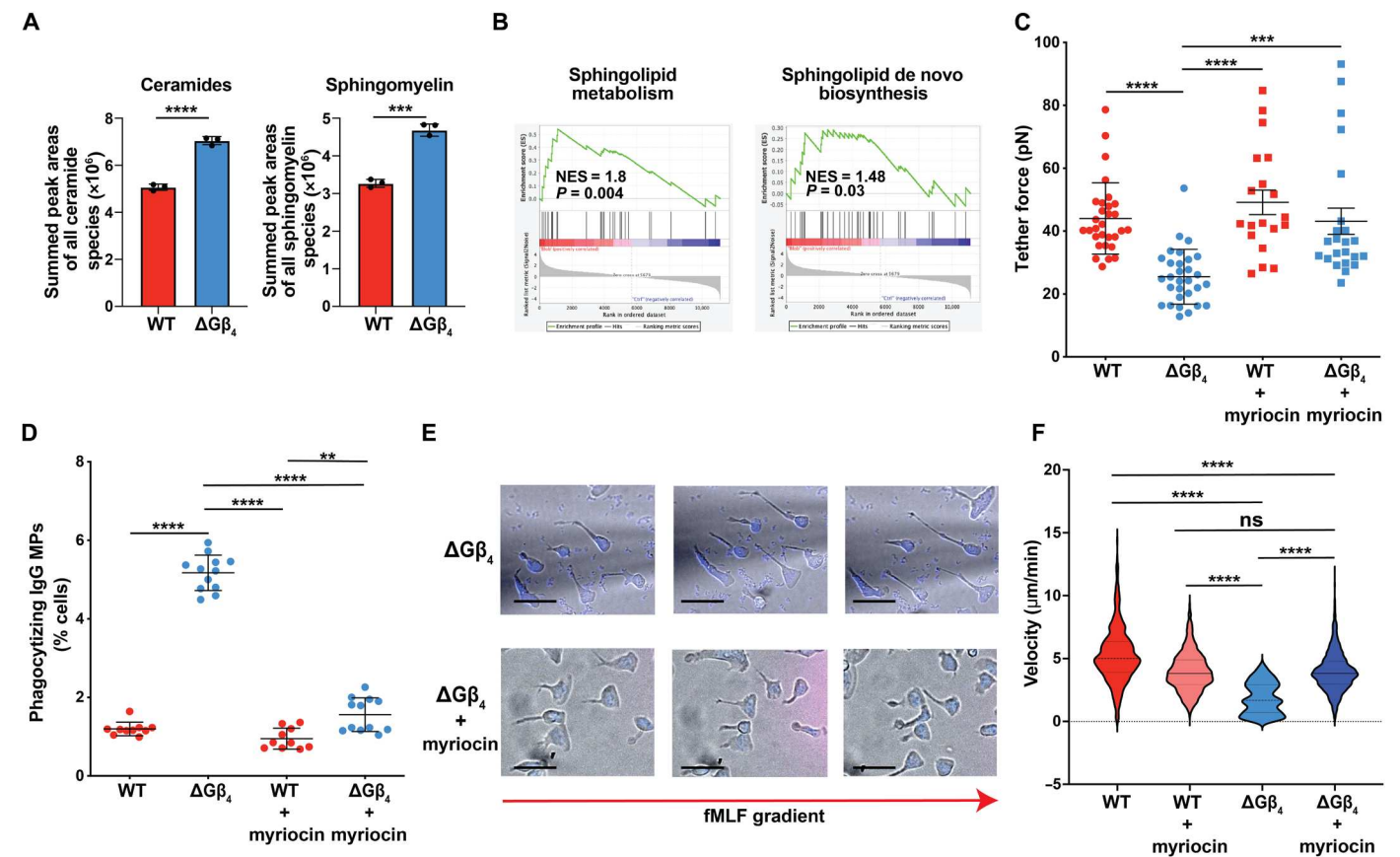


Fig. 5. Gβ₄ regulates plasma membrane expansion via sphingolipid synthesis. (**A**) Lipidomic quantification of ceramides (left) and sphingomyelin (right) in WT and Δ Gβ₄ HL-60 neutrophils. Data are means \pm SD. n=3, pooled from three biological replicates. Unpaired t test, ***P<0.001 and ****P<0.0001. (**B**) Δ Gβ₄ and WT HL-60 neutrophils were compared by RNA sequencing before and after consumption of IgG-coated MPs. Gene set enrichment analysis (GSEA) plots are shown that associate the gene expression changes induced by MP uptake in Δ Gβ₄ cells with gene sets for sphingolipid metabolism (center) and de novo sphingolipid biosynthesis. NES, normalized enrichment score. (**C** to **F**) WT and Δ Gβ₄ HL-60 neutrophils were differentiated in the presence or absence of myriocin and then subjected to biophysical and functional analysis. (C) Quantification of membrane tension, determined by membrane tether pulling. Data represent means \pm SD. $n \ge 19$ for each sample, pooled from five biological replicates. Two-way ANOVA with Šidák's multiple comparisons test, ***P<0.001 and ****P<0.0001. (D) Cells were challenged with IgG-coated MPs, and phagocytosis was quantified after 3 hours. Data represent means \pm SD. $n \ge 10$ for each sample, pooled from five biological replicates. Two-way ANOVA with Šidák's multiple comparisons test, ***P<0.001 and ****P<0.0001. (E) Representative images of myriocin-treated and untreated Δ Gβ₄ HL-60 neutrophils. Scale bars, 10 μm. (F) Migration velocities of myriocin-treated Δ Gβ₄ and WT HL-60 neutrophils. Untreated Δ Gβ₄ and WT velocities from Fig. 3B are included for comparison. Data represent means \pm SD. $n \ge 174$ for each sample, pooled from three biological replicates. One-way ANOVA with Tukey's multiple comparisons test, *****P<0.0001. ns, not significant.

Fluor 633 (AF633), a nondegradable small-molecule dye. Cells that take up FLARE conidia become AF633⁺DsRed⁺, whereas cells that have killed the phagocytized fungi are AF633⁺DsRed⁻ (Fig. 7A) (21). FLARE A. fumigatus infection induced similar levels of neutrophil recruitment to the lungs of WT and Gnb4^{-/-} animals, with CD11b⁺Ly6G⁺SiglecF⁻ cells accounting for ~70% of CD45⁺ infiltrates in both experimental groups (Fig. 7B). However, fungal phagocytosis was almost three times higher in Gnb4^{-/-} neutrophils (Fig. 7C), mirroring the hyperphagic phenotype seen in HL-60 cells, ER-HoxB8 neutrophils, and hiPSC-derived macrophages lacking $G\beta_4$. Among these phagocytic cells, the frequency of fungal killing was unaffected by Gβ₄ deficiency (fig. S12C), consistent with the interpretation that Gβ₄ signaling modulates cargo uptake but not subsequent acidification of the phagolysosome. Gnb4^{-/-} animals also exhibited a ~10-fold reduction in fungal colony-forming units (CFU) in the lung relative to WT controls at the 18-hour time point (Fig. 7D), indicating that the increased conidial phagocytosis conferred by loss of $G\beta_4$ improved fungal clearance during early-stage infection.

Given that $\Delta G\beta_4$ HL-60 neutrophils failed to arrest their motility after cargo uptake in vitro (Fig. 3, C to F), we speculated that $Gnb4^{-/-}$ phagocytes might exhibit altered trafficking behavior in vivo. Accordingly, we examined the organ distribution of phagocytic WT and $Gnb4^{-/-}$ neutrophils 24 hours after FLARE infection (Fig. 7A). In WT mice, neutrophils bearing AF633-labeled material were found predominantly in the lungs, with small numbers in the draining lymph nodes (dLNs) and essentially none in the spleens and blood (Fig. 7, E to G, and fig. S12D). These observations were consistent with the expectation that phagocytosis inhibits motility after conidial uptake in the lungs, thereby preventing the dissemination of neutrophils with internalized pathogens to other organs. By contrast, we observed a substantial number of AF633⁺ neutrophils in the dLNs of $Gnb4^{-/-}$ animals (Fig. 7, E and F), suggesting that $G\beta_4$ deficiency at least partially relieves the brake on motility applied by phagocytosis.

Fig. 6. Gβ₄ deficiency boosts primary macrophage phagocytosis. (A to D) Isogenic $\Delta G\beta_4$ and WT macrophages were derived from hiPSCs and subjected to biophysical and functional assays. (A) Schematic of embryoid body generation from hiPSCs and differentiation of primary macrophages from GMPs. (B and C) Membrane tethers were generated from WT and $\Delta G\beta_4$ macrophages using an optical trap. (B) Quantification of membrane tether force. (C) Quantification of membrane tether length. Data in (B and C) represent means \pm SD. $n \ge 46$ for each sample, pooled from five biological replicates. (D) $\Delta G\beta_4$ and WT macrophages were osmotically shocked and allowed to expand to their full volume to assess total plasma membrane. Data represent means \pm SD. n=12for each sample, pooled from three biological replicates. (**E**) WT and $\Delta G \beta_4$ macrophages were challenged with IgG-coated MPs for 2 hours, and phagocytic uptake was quantified by florescence microscopy. Data represent means \pm SD, pooled from five biological replicates. Unpaired t test (B, C, and E) or two-way ANOVA with Šidák's multiple comparisons test (D), ****P < 0.0001.

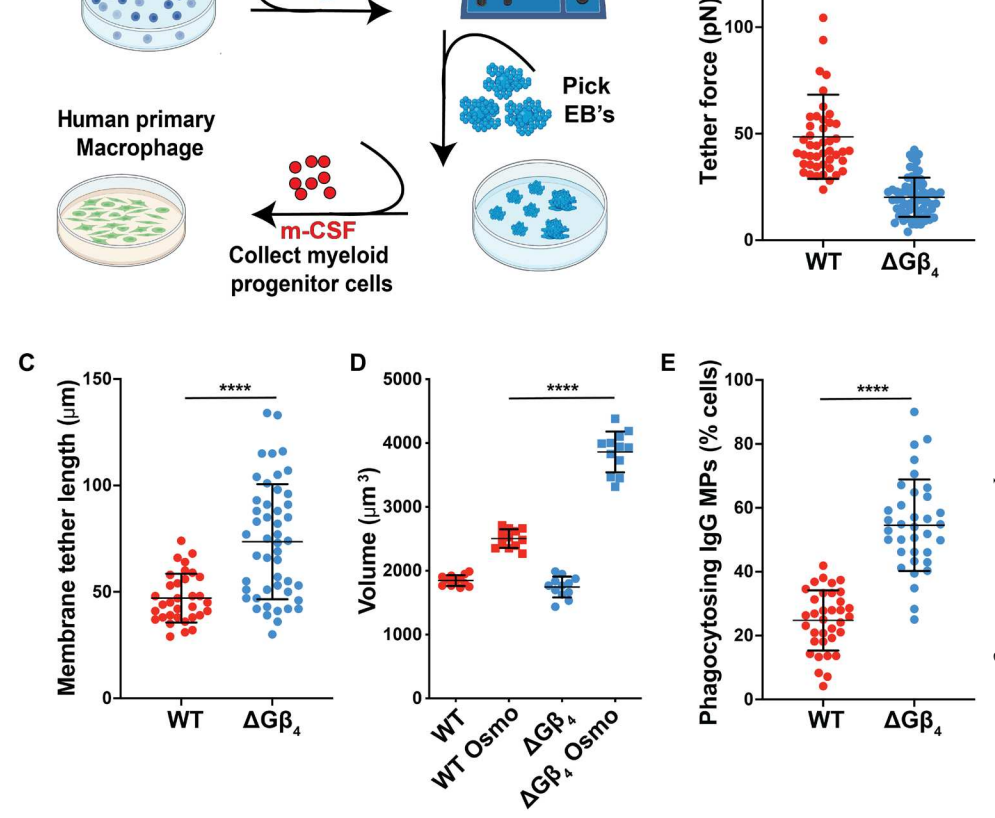
Whereas essentially all AF633⁺ neutrophils in WT dLNs were DsRed⁻, indicating that they had degraded their internalized conidia, a substantial fraction of DsRed⁺AF633⁺ neutrophils were observed in $Gnb4^{-/-}$ dLNs (Fig. 7, E and H). Given that G β_4 deficiency does not affect phagolysosome maturation (fig. S3B), these results strongly suggest that $Gnb4^{-/-}$ neutrophils continue to migrate after conidi-

al uptake, enabling them to reach proximal organs like the dLN before their cargo is broken down. We conclude that $G\beta_4$ deficiency not only increases the phagocytic capacity of myeloid cells in vivo but also disrupts the cross-regulatory relationship between phagocytosis and migration.

To investigate whether the altered behavior of $Gnb4^{-/-}$ neutrophils affected the overall efficacy of antifungal immunity, we infected $Gnb4^{-/-}$ and WT mice with A. fumigatus CEA10, a clinically derived strain with increased pathogenicity in mice (Fig. 7I) (80). WT mice experienced acute weight loss in the first 72 hours after CEA10 administration, and half succumbed to the infection within the first week (Fig. 7, J and K). Both weight loss and mortality were attenuated in $Gnb4^{-/-}$ animals, indicating that loss of $G\beta_4$ protects mice from the adverse effects of A. fumigatus infection.

DISCUSSION

Our results identify $G\beta_4$ as a critical regulator of plasma membrane abundance in myeloid cells and demonstrate that the plasma membrane exerts biophysical control over phagocytic capacity and functional cross-talk. Because the plasma membrane must be mobilized to build protrusive cellular structures, limiting its abundance provides a simple mechanism for not only constraining the magnitude of a given architectural response (e.g., phagocytosis) but also enabling cross-regulation between responses (e.g.,



Initial EB formation

from hiPSC clusters

phagocytosis inhibiting migration). This scarcity model is consistent with prior work documenting antagonism between uptake behaviors, such as phagocytosis and macropinocytosis, and migration (16–18). Thus, the mechanisms governing plasma membrane allocation in myeloid cells effectively dictate their functional potential.

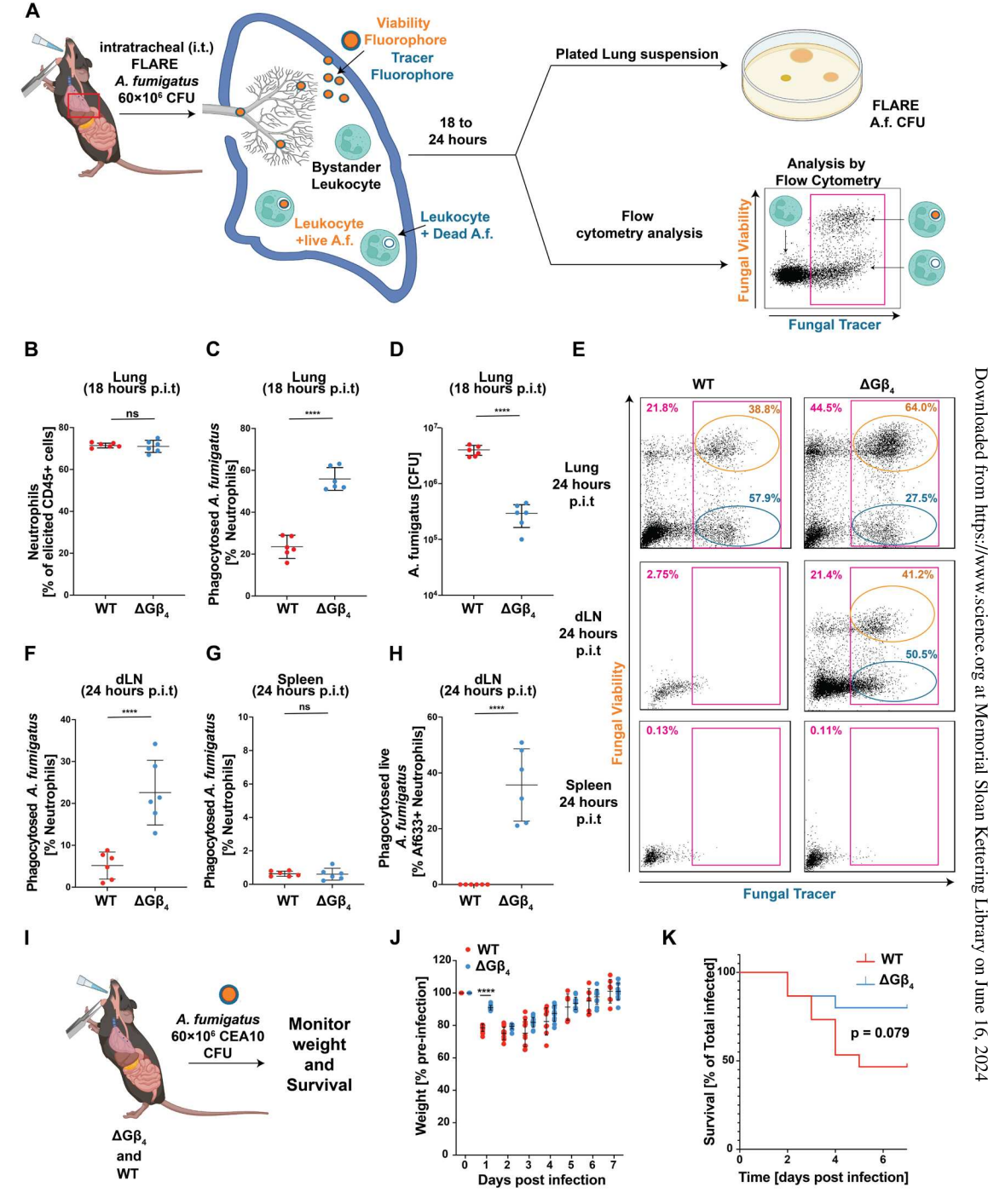
В

150

The plasma membrane–dependent control mechanism studied here appears to most strongly affect the phagocytosis of large (diameter, ~10 μm) cargos, such as apoptotic cells and cancer cells, while having less impact on the uptake of small entities such as bacteria. This distinction likely reflects the fact that engulfing large, unbroken targets with high surface area places a disproportionate burden on plasma membrane mobilization. The importance of $G\beta_4$ for regulating this type of phagocytosis suggests that it may be particularly relevant for processes that involve the clearance of large eukaryotic cells, such as antitumor immunosurveillance and the maintenance of tissue homeostasis.

Although lipid droplets are clearly augmented in $\Delta G\beta_4$ cells, their role in myeloid cell hyperphagia remains unclear. Prior work has associated increased lipid droplet formation with reduced, rather than enhanced, phagocytosis (81–83). In these studies, however, lipid droplet growth either occurred downstream of a genetic defect in phagocytosis itself or was induced by cell-extrinsic nutritional changes, complicating direct comparisons with our findings. Lipid droplets almost exclusively contain triglycerides (84), which must be processed into amphipathic lipids in intracellular

Fig. 7. $G\beta_4$ deficiency boosts phagocytic responses during in vivo fungal infection. (A to **H**) WT and *Gnb4*^{-/-} mice infected with FLARE A. fumigatus were assessed for in vivo phagocytosis and fungal infection after 18 or 24 hours. (A) FLARE conidia express DsRed and are labeled with AF633. Phagocytes become DsRed⁺AF633⁺ upon conidial uptake and then transition to DsRed⁻AF633⁺ as internalized conidia are destroyed. (B) Neutrophil infiltration into the lung 18 hours after infection. (C) Quantification of A. fumigatus phagocytosis by lung neutrophils at the 18-hour time point. (D) Fungal CFU in lung extracts at the 18-hour time point. Data in (B to D) represent means ± SD. n = 6 biological replicates. Unpaired t test, ****P < 0.0001. (E) Representative flow cytometry plots showing neutrophils (CD45+CD11b+Lv6G+) containing FLARE A. fumigatus in the lungs, dLNs, and spleens 24 hours after infection (magenta gates). Gates for neutrophils with live (orange) and dead (blue) conidia are shown. (F) Quantification of neutrophils bearing engulfed FLARE A. fumigatus in the dLNs 24 hours after infection. (G) Quantification of neutrophils bearing engulfed FLARE A. fumigatus in the spleens 24 hours after infection. (H) Quantification of the neutrophils in the dLNs containing live A. fumigatus 24 hours after infection. Data in (F to H) represent means \pm SD. n = 6 biological replicates. Unpaired t test, ****P < 0.0001. (I to K) Gnb4^{-/-} and WT mice were challenged with CEA10 A. fumigatus. (I) Schematic diagram of the experimental approach. Weight (J) and survival (K) of infected mice was monitored over the course of 7 days. Data represent means \pm SD. n = 15 biological replicates. Statistical analy-



sis in (J) was performed using unpaired t test, with ****P < 0.0001. Statistical analysis in (K) performed by logrank test.

organelles before being incorporated into the plasma membrane. Hence, it seems highly unlikely that lipid droplets would augment the plasma membrane directly during phagocytosis. That being said, it has been shown that cells use lipid droplets to buffer membrane depletion and fatigue under conditions of metabolic stress and protein misfolding (84–87). Hence, it is tempting to speculate that the enlarged lipid droplets present in $\Delta G\beta_4$ phagocytes might enable these cells to replenish the plasma

membrane after phagocytosis, thereby facilitating serial consumption.

The notable functional gains exhibited by $\Delta G\beta_4$ neutrophils and macrophages raise the question of why $G\beta_4$ -dependent control of membrane abundance evolved in the first place. One obvious answer is that tight cross-inhibition between phagocytosis and migration is essential for immune function, at least in some contexts. We found that $Gnb4^{-/-}$ neutrophils not only take up more *A. fumigatus* conidia

in vivo but also traffic them out of the lung to the dLN. Although increased fungal dispersion did not appear to compromise immunity in our experiments, one could imagine that a pathogen more capable of resisting or escaping the phagolysosome could exploit the dysregulated migration of $G\beta_4$ -deficient phagocytes to spread.

Although we cannot, at present, rule out a role for $G\beta_4$ in the acute regulation of phagocytosis and motility, we favor a model in which the Gβ₄ pathway acts during myeloid cell differentiation to dictate the size and composition of the plasma membrane, which then serves as a master mechanoregulator of morphology and effector responses in the terminally differentiated state (fig. S13). This model is consistent with our observations that $\Delta G\beta_4$ neutrophils and macrophages exhibit architectural abnormalities (Fig. 4 and fig. S6) and that acute myriocin treatment fails to reverse the $\Delta G\beta_4$ phagocytosis phenotype (fig. S9F). Conceptually, the regulation of plasma membrane abundance by Gβ₄ signaling is analogous to how the unfolded protein response sets the size of the endoplasmic reticulum and, therefore, the capacity to process misfolded proteins under conditions of cell stress (88). We postulate that differential Gβ₄ expression among myeloid progenitors might promote functional diversification by enabling the formation of differentiated subsets with a spectrum of plasma membrane-defined phagocytic and migratory set points. This type of diversity could enable the innate immune system to engage effectively with a wide variety of homeostatic and microbial challenges.

 $G\beta_4$ mutations have been associated with Charcot-Marie-Tooth disease (CMTD) (89–92), a hereditary neurological disorder characterized by the progressive demyelination of peripheral nerves. Although the pathogenesis of this disease is generally thought to arise from cell-intrinsic glial dysfunction, macrophages routinely patrol peripheral nerves and are well positioned to induce autoimmune neuropathy (93, 94). Macrophage depletion has been shown to attenuate neurodegeneration in mouse CMTD models (95–97). In light of these reports, our data raise the intriguing possibility that dysregulated macrophage phagocytosis might contribute to at least some forms of CMTD.

The identification of $G\beta_4$ signaling and sphingolipid synthesis as key regulators of phagocytic capacity in myeloid cells reveals heretofore unexplored avenues for enhancing innate immunity in therapeutic contexts. By targeting the architectural basis of cargo uptake, one could potentially modulate phagocyte activity in a manner that is agnostic to specific targets. We anticipate that an approach like this would be particularly useful for treating systemic microbial infections and for enhancing the antitumor potential of chimeric antigen receptor (CAR)–macrophages (10, 98). Exploring these possibilities in translationally relevant experimental systems will be an interesting topic for future research.

MATERIALS AND METHODS

Study design

The goal of this study was to determine how $G\beta_4$ signaling affects myeloid cell phagocytosis and migration. In vitro assays were used to measure phagocytic uptake and chemotaxis. FIB-SEM was used for ultrastructural analysis of the cell membrane, and optical trap methodology was used to quantify membrane tension. We also applied lipidomics/mass spectrometry and RNA sequencing to investigate the molecular basis of the $\Delta G\beta 4$ phenotype. Experimental sample sizes were not predetermined, and there were no predefined study end points. Experiments were not randomized, and

investigators were not blinded during data acquisition and analysis. In general, experiments were performed at least three times (three biological replicates). Specific information about replication is included in the figure legends. Data analysis protocols are detailed below and in the Supplementary Materials.

HL-60 genetic manipulation

Gβ isoforms were deleted from HL-60 progenitors using the IDT Alt-R CRISPR-Cas9 system (IDT). Briefly, crispr (cr)RNAs specific for each Gβ isoform (see table S1 for sequence details) were resuspended in sterile duplex buffer (IDT) to a final concentration of 200 μM. Each crRNA was then mixed with tracrRNA-ATTO 550 (IDT) at a 1:1 ratio and annealed to form sgRNA using a thermocycler (Bio-Rad). sgRNA:Cas9 ribonucleoprotein (RNPs) were formed by mixing 0.3 µl of 36 µM Cas9 protein (IDT) with annealed sgRNAs at a 1:1 ratio followed by room temperature incubation for 10 to 20 min. HL-60 progenitor cells at a density of 2.2×10^6 (>95% viability) were washed with phosphate-buffered saline (PBS) and then transferred into 200 µl of resuspension buffer (Buffer R, Invitrogen). The cells were then mixed with RNPs, loaded into an electroporation cuvette (Thermo Fisher Scientific) with E2 buffer, and electroporated at 1350 V for 35 s. Electroporated cells were recovered in 2 ml of RPMI with 20% fetal bovine serum (FBS) and 1% penicillinstreptomycin and incubated at 37°C and 5% CO₂ for 24 to 48 hours. Subsequently, ATTO 550-positive cells were single-cell sorted into 96-well plates using a FACS Aria 3. Cell clones were screened for Gβ gene expression after 2 to 3 weeks. For screening, cells were fixed and permeabilized using BD fixation and permeabilization buffers, followed by staining using primary antibodies against Gβ isoforms (table S2) at a dilution 1:100 for 30 min at 4°C. Cells were then stained with goat anti-rabbit AF647 antibody (Thermo Fisher Scientific) for 20 min at room temperature before flow cytometric analysis on a CytoFLEX LX machine (Beckman Coulter).

To overexpress $G\beta_4$, a *GNB4* gene block (IDT) containing homology arms to the lentiviral vector pLVX-Puro (Clontech) was inserted into Xho I-digested pLVX-Puro using the In-Fusion HD Kit (Takara Bio). The homology arms were 5'-ctaccggactcagatctcga-3' at the 5' end of GNB4 and 5'-tcgagctcatcgggatcccgctcgacta-3' at the 3' end. The resulting plasmid was combined with plasmids encoding (i) gagpol from HIV53 and (ii) appropriate viral glycoproteins (vesicular stomatitis virus glycoprotein), and the mixture then transfected into human embryonic kidney (HEK) 293T Lenti-X cells (Takara Bio) using the X-tremeGENE transfection reagent (Roche Applied Science). Lentivirus was collected 24 and 48 hours after transfection and stored at -80° C until use. For transduction, 0.5×10^{6} to 1×10^{6} HL-60 progenitor cells were mixed with lentivirus preparations (1 ml of virus supplemented with polybrene and Hepes) and centrifuged at 1400g at 37°C for 2 hours in either 24-well or 6-well polystyrene plates (Corning). Subsequently, 1 ml of RPMI complete media (10% FBS and 1% penicillin-streptomycin) was added to the cells, followed by overnight incubation at 37°C and 5% CO₂. Cells were then placed in puromycin (0.5 µg/ml) for 14 days to select for successfully transduced cells. HL-60 progenitors transduced with lentivirus derived from empty pLVX-Puro were prepared in parallel as controls. To express F-tractin-mCherry in HL-60 cells, DNA encoding the F-tractin-mCherry fusion was amplified from a C1-F-tractin-mCherry plasmid (Addgene, #155218) and then subcloned into the lentiviral vector pLVX-M-Puro (Clontech) by Gibson reaction. Lentivirus production and transduction were

performed as described above. To express PH-AKT-BFP in HL-60 cells, DNA encoding the PH domain of AKT was amplified from a PH-AKT-Venus plasmid (Plasmid #85223), and DNA encoding BFP was from pLentiCas9-BFP (Plasmid #78545). The fragments were then subcloned into the lentiviral vector pHR using the Gibson approach.

Flow cytometric MP phagocytosis assay

Neutrophils stained with either Hoechst or CellVue Maroon (both from Thermo Fisher Scientific) were seeded into fibronectin-coated 24-well plates at a density of 150,000 cells per well. FITC/LRBlabeled MPs coated with a phagocytic target ligand (e.g., IgG) were then added at a 1:2 (MP:cell) ratio, followed by incubation at 37°C and 5% CO₂ for 3 hours. In certain experiments, neutrophils were pretreated with 1 µM PIK90 (Tocris Biosciences) for 30 min before MP addition and maintained in 1 µM PIK90 for the duration of the 3-hour coincubation. Cells were then removed from the surface by trypsinization and transferred into fluorescence-activated cell sorting (FACS) tubes for analysis using a CytoFLEX LX machine (Beckman Coulter). Analysis was performed by first gating out freefloating MPs and then identifying LRB⁺FITClow cells, indicative of successful uptake and acidification of MPs. In each sample, the total number of LRB⁺FITC^{low} cells was normalized to the total number of live cells to generate a %phagocytosis metric. In experiments using pHrodo Green-or pHrodo Red-dyed MPs, the %phagocytosis metric was calculated using pHrodo Bright cells [in FITC or phycoerythrin (PE) channels] as the numerator and total cells as the denominator. In experiments comparing $\Delta G\beta_4$ and WT HL-60 cells in the same sample, each cell type was labeled with a different dye (either Hoechst or CellVue Maroon, both from Thermo Fisher Scientific) to distinguish them during end point flow cytometric analysis. Dyes were switched between experiments to control for potential effects of the dyes on phagocytosis.

Wide-field imaging of MP phagocytosis

Neutrophils or macrophages were stained using Hoechst and/or CellVue Maroon (both from Thermo Fisher Scientific) and seeded into fibronectin-coated eight-well chamber slides (ibidi) at a density of 100,000 or 50,000 cells per well, respectively. FITC/LRB-labeled IgG-coated MPs were then added at a 1:2 (MP:cell) ratio, and the samples were imaged on a Zeiss Axiovert microscope using a 20× objective lens for at least 2 hours at 1-min intervals. 4',6-Diamidino-2-phenylindole, FITC, and tetramethyl rhodamine isothiocyanate images were collected at each time point. Phagocytosed MPs were identified in Fiji by a reduction in FITC signal due to phagolysosome acidification. %Phagocytosis was determined by dividing the number of phagocytes containing acidified MPs by the total number of phagocytes in each frame.

Micropipette migration assay

Differentiated $\Delta G\beta 4$ and WT HL-60 neutrophils were stained with Hoechst (Thermo Fisher Scientific) for 20 min at 25°C and allowed to attach to fibronectin-coated 35-mm glass-bottom cover slips for 1 hour (250,000 cells per dish). Samples were washed to remove nonadherent cells and left in 3 ml of complete RPMI media before imaging. A femptotip (Eppendorf) micropipette loaded with sterile filtered RPMI containing 2% fatty acid–free bovine serum albumin, 1% penicillin-streptomycin, 200 nM fMLF, and trace AF647 dye was attached to a FemptoJet 4i (Eppendorf), and the micropipette tip was positioned at the center of the imaging frame. Pressure (400 psi)

was then applied to dispense the chemoattractant mixture, and serial images (40-s intervals between frames) were collected over the course of an hour at 20× magnification using a Ti Eclipse microscope with a CSU-0W1 Yokogawa camera (Nikon) at 37°C and 5% CO₂. To measure migration after MP uptake, Δ Gβ4 and WT HL-60 cells were preincubated with pHrodo Green–or pHrodo Red–labeled MPs, respectively, for 3 hours. Cells that had taken up MPs during this time were FACS-sorted on the basis of green (Δ Gβ4) or red (WT) fluorescence. A 1:1 mixture of these cells was then applied to fibronectin-coated cover slips (250,000 cells per dish) and chemotaxis toward a point source of fMLF measured as described above.

FIB-SEM imaging and analysis

Cells were plated on Aclar coverslips coated with fibronectin and then fixed with 2% glutaraldehyde and 2 mM CaCl₂ in 0.08 M sodium cacodylate buffer (pH 7.2). This primary fixation was followed by a reduced osmium-thiocarbohydrazide-osmium protocol as follows: Cells were incubated for 1 hour in 1% OsO₄ and 1.25% potassium ferrocyanide in 0.1 M sodium cacodylate buffer on ice, washed with buffer, and then incubated with 1% thiocarbohydrazide in water for 12 min. After washing, cells were treated with 1% osmium tetroxide in 0.1 M cacodylate buffer for 30 min on ice. The samples were then dehydrated using a graded series of ethanol solutions and embedded in Eponate 12. Sample blocks were trimmed and then mounted on an SEM sample holder using double-sided carbon tape (EMS). Colloidal silver paint (EMS) was used to electrically ground the sides of the resin block. The entire surface of the specimen was then sputter-coated with a thin layer (5 nm) of gold/palladium. The sample was imaged using immersion, through-the-lens detector, back-scattered electron mode on an FEI Helios Nanolab 650 microscope. Images were recorded after each round of ion beam milling using the SEM beam at 2.0 keV and 0.10-nA current with a working distance of <5 mm. The ion beam was held at 30 keV, with a milling current of 80 pA. Data acquisition occurred through automation using Auto Slice and View G3 software. Raw images were 4096 pixels by 2048 pixels, with 20- to 50-nm slices viewed at a -38° crosssectional angle. Each raw image had a horizontal field width of 10 to 15 μm with an XY pixel size of 2 to 4 nm and a 40-nm Z-step size. Images were aligned using the image processing programs in IMOD. All segmentation was performed using semimanual thresholding and manual annotation of a test set (10% of data) using the LABKIT machine learning plug-in for Imaris. Three-dimensional renderings, reconstructions, surface/volume calculations, and internal vesicle volume calculations were performed using Imaris (Bitplane).

Myriocin sphingolipid synthesis inhibition assays

For acute myriocin treatment, HL-60 cells on the fifth day of DMSO differentiation were treated with a final concentration of 50 nM myriocin (Millipore Sigma-Aldrich) for 12 hours before phagocytosis or C-trap experiments. For long-term inhibition of sphingolipid synthesis, HL-60 progenitor cells were incubated over the 5-day DMSO differentiation in the presence of 50 nM myriocin. Treated cells were then used in phagocytosis, migration, or C-trap experiments. No observable effect on viability was observed in either treatment regime.

Osmotic shock experiments

HL-60 cells or terminally differentiated primary human macrophages (derived from hiPSC cells) were suspended in 200 μl of complete

RPMI (supplemented with 10% FBS and 1% penicillin-streptomycin) containing either 1.5% DMSO or 50 ng/ml human macrophage colony stimulating factor (h-mCSF), respectively, and then applied to a Vi Cell Blue (Beckman Coulter, MA) cell counter to measure cell diameter. The samples were then osmotically shocked for 2 or 4 min by adding 180 μl of sterile ddH $_2O$ to 20 μl of suspended cells (final concentration of 2 \times 10^5 cells/ml) before loading onto the same device. Each measurement was performed using nine biological replicates. All recorded samples had >90% viability during the assay, as monitored by trypan blue (Thermo Fisher Scientific) exclusion.

Membrane tension measurements

Plasma membrane tension was quantified using a C-Trap optical trapping device (Lumicks BV, Netherlands). An infrared laser beam (50 mW and 1064 nm) was tightly focused through a series of mirrors, beam expanders, and a high-numerical aperture (NA) objective lens (63×/1.2 NA; Nikon Instruments) to form a steerable optical trap. Cells were immobilized inside an Ibidi μ-slide (Ibidi GmbH, Germany) treated with fibronectin (200 µg/ml; Thermo Fisher Scientific/Sigma-Aldrich). To measure plasma membrane tension, polystyrene beads (2.2 µm; Spherotech Inc., IL) were coated with concanavalin A (50 μg/ml; Thermo Fisher Scientific/Sigma-Aldrich) and added to the cell culture medium inside the slide. Beads were momentarily placed in contact with the cell membrane, and tethers were then extruded by moving the bead away from the cell perpendicularly at a speed of 2 $\mu m/s$. Force measurements were made using the Lumicks Bluelake software suite by capturing the exiting trapping light with a high-NA condenser lens (63×/1.45, oil immersion; Zeiss AB, Germany) and measuring bead displacement in the trap with position-sensitive detectors through back focal plane interferometry. Membrane tether breaking was documented as a sharp discontinuity in tether force during tether extrusion, with breaking distance measured from simultaneously collected brightfield images using Fiji. Data analysis was performed using Python 3.8.0.

Lipidomics

Frozen cell pellets were thawed and extracted using a modified Folch protocol (99). Briefly, samples were resuspended in 300 µl of methanol containing SPLASH LIPIDOMIX (Avanti Polar Lipids) as internal standards, vortexed, and then mixed with 600 µl of chloroform. Water (180 µl) was added to each tube to induce phase separation, and after mixing, samples were centrifuged at 16,000g for 5 min at 4°C. Subsequently, the lower chloroform layer was collected and the aqueous layer reextracted using 450 µl of chloroform:methanol:water (3:48:47 v/v/v). The lower chloroform layer was collected and pooled with the previous extract. Samples were then dried under nitrogen at 40°C and resuspended in 100 μl of 90:10 methanol:chloroform. Lipid profiling was performed using an Agilent 6546 Q-TOF mass spectrometer in positive and negative ionization modes, coupled to a ZORBAX Eclipse Plus C-18 column (100 mm by 2.1 mm; 1.8-µm particle size; Agilent). Mobile phase A consisted of 10 mM ammonium formate in 50:30:20 water:acetonitrile:isopropanol. Mobile phase B consisted of 10 mM ammonium formate in 1:9:90 water:acetonitrile:isopropanol. Liquid chromatography (LC) gradient conditions were as follows: 0 min at 0% B, 2.7 min at 45% B, 2.8 min at 53% B, 9 min at 65% B, 9.10 min at 89% B, 11 min at 92% B, 11.10 min 100% B, 12 min at 10% B, and 15 min at 10% B. Other LC parameters were as follows: flow rate at 0.4 ml/min, column temperature at 60°C, and

injection volume of 5 μ l. Mass spectrometry (MS) source parameters included were as follows: gas temperature, 200°C; gas flow, 10 liter/min; nebulizer pressure, 50 psi; sheath gas temperature, 300°C; sheath gas flow, 12 liter/min; Vcap, 3000 V; nozzle voltage, 0 V; and fragmentor, 150 V. For lipid annotation, five injections of iterative tandem MS (MS/MS) acquisition were performed on a pooled lipid extract in both positive and negative polarity. To identify lipid species, iterative MS/MS acquisition data in positive and negative polarity was processed using Agilent Lipid Annotator software 1.0 (100). Subsequent targeted feature extraction and peak integration was performed using Skyline (101). For statistical analysis, the Welch t test was used for pairwise comparisons between WT and $\Delta G \beta_4$ groups with Benjamini-Hochberg false discovery rate correction.

Generation of Gnb4^{-/-} mice

The animal protocols used for this study were approved by the Institutional Animal Care and Use Committee of Memorial Sloan Kettering Cancer Center (MSKCC). Two sgRNAs (with targeting sequences 5'-cgtcaaaatatcgcaagtgc-3' and 5'-aggtgtcagatcaaacc-3') against exon 4 of the *Gnb4* locus (IDT) were injected together with purified Cas9 protein (IDT) into C57BL/6 zygotes, which were then transferred into C57BL/6 pseudopregnant females. Founder animals were screened for deletion of the entire exon 4 and the presence of an early stop codon in exon 5 and then bred to homozygosity. Routine genotyping polymerase chain reactions were performed using forward (5'-ggagaacagctagtactcttaac-3') and reverse (5'-aaaagtatttattagcagtatc-3') primers. The resulting amplicons for WT and *Gnb4* KO mutant alleles were 1360 and 305 base pairs, respectively.

A. fumigatus FLARE intratracheal mouse fungal infections

Gnb4^{-/-} and WT mice were infected by intratracheal administration of 60×10^6 FLARE Af293 A. fumigatus (see Supplementary Materials and Methods for the staining protocol) in 50 µl. WT mice were also infected with unlabeled A. fumigatus to serve as analysis controls (see below). Eighteen hours after infection, mice were euthanized, and their lungs were harvested into 5 ml of digestion buffer [PBS with 5% FBS, deoxyribonuclease I (0.1 mg/ml), and type IV collagenase (Worthington) at 2.2 mg/ml]. Tissue homogenization was performed using a MACS Octo Dissociator for 55 s at 1302 rpm, followed by slow rotation at 37°C for 40 min. A final mechanical homogenization was performed for 37 s at 2079 rpm, after which all samples were diluted with 5 ml of PBS + 5% FBS, filtered through a 100-μm pore size cell strainer, and centrifuged at 300g for 5 min at 4°C. The pellet was resuspended in 2 ml of ACK lysis buffer (BD) and incubated for 15 min to achieve red blood cell lysis. After quenching in 4 ml of RPMI + 10% FBS, cells were centrifuged at 300g for 5 min at 4°C, followed by resuspension in cold FACS buffer (PBS + 5% FBS). To assess dissemination at 24 hours after infection, lungs, dLNs, spleens, and 200 µl of blood were harvested from each mouse. Lungs were processed as described above. dLNs and spleens were homogenized and filtered through a 100-µm pore size cell strainer. Subsequently, the spleen single-cell suspension was centrifuged, resuspended in 2 ml of ACK lysis buffer (BD), and incubated for 15 min to achieve red blood cell lysis. After quenching in 4 ml of RPMI + 10% FBS, cells were centrifuged at 300g for 5 min at 4°C, followed by resuspension in cold FACS buffer. Blood samples were diluted into 2 ml of ACK lysis buffer (BD) containing 100 mM EDTA and incubated for 15 min to achieve red blood cell lysis. After quenching in 4 ml of

RPMI + 10% FBS, cells were centrifuged at 300g for 5 min at 4°C, followed by resuspension in cold FACS buffer. Aliquots of 2×10^6 cells from each organ were dispensed into round-bottom 96-well plates (Corning) and then stained for 20 min at 4°C with a viability dye (1:250; Tonbo Ghost Dye Violet 510) along with antibodies against Ly6G (BUV395, 1:100), CD11b (BUV805, 1:100), Siglec F (BV650, 1:100), CD45 (BV785), and CD11c (PE-Cy7, 1:100; table S3). Samples were then applied to a CytoFLEX LX flow cytometer and analyzed using FlowJo software. Neutrophils were identified as CD 11b⁺Ly6G⁺SiglecF⁻CD11c⁻ cells. %Phagocytosis was determined by dividing the total number of AF633⁺ neutrophils in each sample by the total number of neutrophils. %FLARE killing was expressed as the number of AF633⁺DsRed⁻ neutrophils over the total number of AF633⁺ neutrophils in each sample. Gating for AF633⁺ neutrophils was facilitated using unlabeled neutrophils extracted from mice infected with unlabeled A. fumigatus. To quantify fungal infection, lung suspensions were diluted 50-fold, and 50 µl of each sample was plated on Sabouraud dextrose agar (Thermo Fisher Scientific). CFUs were quantified after 2 days of incubation at 37°C. For survival experiments, both *Gnb4*^{-/-} and WT mice were infected with CEA10 A. fumigatus (65 \times 10⁶ CFU). Weight and survival were monitored over the course of 7 days.

Statistical analysis

Figure panels show either representative images or data pooled from all biological replicates. *t*, one- or two-way analysis of variance (ANOVA), and logrank testing was performed as indicated using Prism. Error bars denote SD or SEM as described in the figure legends.

Supplementary Materials

This PDF file includes: Materials and Methods Figs. S1 to S13 Tables S1 to S3 References (102–108)

Other Supplementary Material for this manuscript includes the following:

Data files S1 and S2 Movies S1 to S3 MDAR Reproducibility Checklist

REFERENCES AND NOTES

- J. Wang, M. Hossain, A. Thanabalasuriar, M. Gunzer, C. Meininger, P. Kubes, Visualizing the function and fate of neutrophils in sterile injury and repair. Science 358, 111–116 (2017).
- M. Peiseler, P. Kubes, More friend than foe: The emerging role of neutrophils in tissue repair. J. Clin. Invest. 129, 2629–2639 (2019).
- A. R. Witter, B. M. Okunnu, R. E. Berg, The essential role of neutrophils during infection with the intracellular bacterial pathogen *Listeria monocytogenes*. J. Immunol. 197, 1557–1565 (2016).
- E. Pylaeva, G. Korschunow, I. Spyra, S. Bordbari, E. Siakaeva, I. Ozel, M. Domnich, A. Squire, A. Hasenberg, K. Thangavelu, T. Hussain, M. Goetz, K. S. Lang, M. Gunzer, W. Hansen, J. Buer, A. Bankfalvi, S. Lang, J. Jablonska, During early stages of cancer, neutrophils initiate anti-tumor immune responses in tumor-draining lymph nodes. *Cell Rep.* 40, 111171 (2022).
- C. Li, A. Ebrahimi, H. Schluesener, Drug pipeline in neurodegeneration based on transgenic mice models of Alzheimer's disease. Ageing Res. Rev. 12, 116–140 (2013).
- 6. S. Gordon, Phagocytosis: An immunobiologic process. *Immunity* **44**, 463–475 (2016).
- S. F. Yanuck, Microglial phagocytosis of neurons: Diminishing neuronal loss in traumatic, infectious, inflammatory, and autoimmune CNS disorders. Front. Psych. 10, 712 (2019).
- 8. D. M. Schrijvers, G. R. Y. De Meyer, A. G. Herman, W. Martinet, Phagocytosis in atherosclerosis: Molecular mechanisms and implications for plaque progression and stability. *Cardiovasc. Res.* **73**, 470–480 (2007).
- F. Abdolmaleki, N. Farahani, S. M. Gheibi Hayat, M. Pirro, V. Bianconi, G. E. Barreto,
 A. Sahebkar, The role of efferocytosis in autoimmune diseases. Front. Immunol. 9, 1645 (2018).

- C. Alvey, D. E. Discher, Engineering macrophages to eat cancer: From "marker of self" CD47 and phagocytosis to differentiation. J. Leukoc. Biol. 102, 31–40 (2017).
- L. J. Dooling, J. C. Andrechak, B. H. Hayes, S. Kadu, W. Zhang, R. Pan, M. Vashisth, J. Irianto, C. M. Alvey, L. Ma, D. E. Discher, Cooperative phagocytosis of solid tumours by macrophages triggers durable anti-tumour responses. *Nat. Biomed. Eng.* 7, 1081–1096 (2023).
- J. C. Andrechak, L. J. Dooling, D. E. Discher, The macrophage checkpoint CD47: SIRPα for recognition of 'self' cells: From clinical trials of blocking antibodies to mechanobiological fundamentals. *Philos. Trans. R. Soc. Lond. B Biol. Sci.* 374, 20180217 (2019).
- C. Johansson, F. C. M. Kirsebom, Neutrophils in respiratory viral infections. *Mucosal Immunol.* 14, 815–827 (2021).
- V. Jaumouille, C. M. Waterman, Physical constraints and forces involved in phagocytosis. Front. Immunol. 11, 1097 (2020).
- S. Mylvaganam, S. A. Freeman, S. Grinstein, The cytoskeleton in phagocytosis and macropinocytosis. Curr. Biol. 31, R619–R632 (2021).
- M. Bretou, P. J. Saez, D. Sanseau, M. Maurin, D. Lankar, M. Chabaud, C. Spampanato, O. Malbec, L. Barbier, S. Muallem, P. Maiuri, A. Ballabio, J. Helft, M. Piel, P. Vargas, A.-M. Lennon-Dumenil, Lysosome signaling controls the migration of dendritic cells. Sci. Immunol. 2, eaak9573 (2017).
- M. Chabaud, M. L. Heuze, M. Bretou, P. Vargas, P. Maiuri, P. Solanes, M. Maurin, E. Terriac, M. Le Berre, D. Lankar, T. Piolot, R. S. Adelstein, Y. Zhang, M. Sixt, J. Jacobelli, O. Benichou, R. Voituriez, M. Piel, A. M. Lennon-Dumenil, Cell migration and antigen capture are antagonistic processes coupled by myosin II in dendritic cells. *Nat. Commun.* 6, 7526 (2015).
- Y. Luo, B. M. Isaac, A. Casadevall, D. Cox, Phagocytosis inhibits F-actin-enriched membrane protrusions stimulated by fractalkine (CX3CL1) and colony-stimulating factor 1. Infect. Immun. 77, 4487–4495 (2009).
- N. Branzk, A. Lubojemska, S. E. Hardison, Q. Wang, M. G. Gutierrez, G. D. Brown,
 V. Papayannopoulos, Neutrophils sense microbe size and selectively release neutrophil extracellular traps in response to large pathogens. *Nat. Immunol.* 15, 1017–1025 (2014).
- B. G. Yipp, B. Petri, D. Salina, C. N. Jenne, B. N. V. Scott, L. D. Zbytnuik, K. Pittman, M. Asaduzzaman, K. Wu, H. C. Meijndert, S. E. Malawista, A. de Boisfleury Chevance, K. Zhang, J. Conly, P. Kubes, Infection-induced NETosis is a dynamic process involving neutrophil multitasking in vivo. *Nat. Med.* 18, 1386–1393 (2012).
- A. Jhingran, K. B. Mar, D. K. Kumasaka, S. E. Knoblaugh, L. Y. Ngo, B. H. Segal, Y. Iwakura, C. A. Lowell, J. A. Hamerman, X. Lin, T. M. Hohl, Tracing conidial fate and measuring host cell antifungal activity using a reporter of microbial viability in the lung. *Cell Rep.* 2, 1762–1773 (2012).
- A. Hopke, A. Scherer, S. Kreuzburg, M. S. Abers, C. S. Zerbe, M. C. Dinauer, M. K. Mansour, D. Irimia, Neutrophil swarming delays the growth of clusters of pathogenic fungi. *Nat. Commun.* 11, 2031 (2020).
- B. Hamza, E. Wong, S. Patel, H. Cho, J. Martel, D. Irimia, Retrotaxis of human neutrophils during mechanical confinement inside microfluidic channels. *Integr. Biol.* 6, 175–183 (2014).
- 24. E. Uribe-Querol, C. Rosales, Phagocytosis: Our current understanding of a universal biological process. *Front. Immunol.* **11**, 1066 (2020).
- D. Vorselen, R. L. D. Labitigan, J. A. Theriot, A mechanical perspective on phagocytic cup formation. Curr. Opin. Cell Biol. 66, 112–122 (2020).
- N. Jain, J. Moeller, V. Vogel, Mechanobiology of macrophages: How physical factors coregulate macrophage plasticity and phagocytosis. *Annu. Rev. Biomed. Eng.* 21, 267–297 (2019).
- K. M. Adlerz, H. Aranda-Espinoza, H. N. Hayenga, Substrate elasticity regulates the behavior of human monocyte-derived macrophages. *Eur. Biophys. J.* 45, 301–309 (2016)
- A. K. Blakney, M. D. Swartzlander, S. J. Bryant, The effects of substrate stiffness on the in vitro activation of macrophages and in vivo host response to poly(ethylene glycol)based hydrogels. J. Biomed. Mater. Res. A 100, 1375–1386 (2012).
- T. Okamoto, Y. Takagi, E. Kawamoto, E. J. Park, H. Usuda, K. Wada, M. Shimaoka, Reduced substrate stiffness promotes M2-like macrophage activation and enhances peroxisome proliferator-activated receptor γ expression. *Exp. Cell Res.* 367, 264–273 (2018).
- D. M. Underhill, H. S. Goodridge, Information processing during phagocytosis. Nat. Rev. Immunol. 12, 492–502 (2012).
- N. G. Sosale, T. Rouhiparkouhi, A. M. Bradshaw, R. Dimova, R. Lipowsky, D. E. Discher, Cell rigidity and shape override CD47's "self"-signaling in phagocytosis by hyperactivating myosin-II. *Blood* 125, 542–552 (2015).
- L. Bajno, X. R. Peng, A. D. Schreiber, H. P. Moore, W. S. Trimble, S. Grinstein, Focal exocytosis of VAMP3-containing vesicles at sites of phagosome formation. *J. Cell Biol.* 149, 697–706 (2000).

SCIENCE IMMUNOLOGY | RESEARCH ARTICLE

- V. Braun, V. Fraisier, G. Raposo, I. Hurbain, J. B. Sibarita, P. Chavrier, T. Galli, F. Niedergang, TI-VAMP/VAMP7 is required for optimal phagocytosis of opsonised particles in macrophages. *EMBO J.* 23, 4166–4176 (2004).
- D. J. Hackam, O. D. Rotstein, C. Sjolin, A. D. Schreiber, W. S. Trimble, S. Grinstein, v-SNARE-dependent secretion is required for phagocytosis. *Proc. Natl. Acad. Sci. U.S.A.* 95, 11691–11696 (1998).
- B. Peracino, J. Borleis, T. Jin, M. Westphal, J. M. Schwartz, L. Wu, E. Bracco, G. Gerisch, P. Devreotes, S. Bozzaro, G protein beta subunit-null mutants are impaired in phagocytosis and chemotaxis due to inappropriate regulation of the actin cytoskeleton. J. Cell Biol. 141, 1529–1537 (1998).
- X. Wen, X. Xu, W. Sun, K. Chen, M. Pan, J. M. Wang, S. M. Bolland, T. Jin, G-protein-coupled formyl peptide receptors play a dual role in neutrophil chemotaxis and bacterial phagocytosis. *Mol. Biol. Cell* 30, 346–356 (2019).
- M. Pan, X. Xu, Y. Chen, T. Jin, Identification of a chemoattractant G-protein-coupled receptor for folic acid that controls both chemotaxis and phagocytosis. *Dev. Cell* 36, 428–439 (2016).
- A. Cohen, E. E. Jeng, M. Voorhies, J. Symington, N. Ali, R. A. Rodriguez, M. C. Bassik, A. Sil, Genome-scale CRISPR screening reveals that C3aR signaling is critical for rapid capture of fungi by macrophages. *PLOS Pathog.* 18, e1010237 (2022).
- R. A. Kamber, Y. Nishiga, B. Morton, A. M. Banuelos, A. A. Barkal, F. Vences-Catalán, M. Gu, D. Fernandez, J. A. Seoane, D. Yao, K. Liu, S. Lin, K. Spees, C. Curtis, L. Jerby-Arnon, I. L. Weissman, J. Sage, M. C. Bassik, Inter-cellular CRISPR screens reveal regulators of cancer cell phagocytosis. *Nature* 597, 549–554 (2021).
- 40. K. M. Yamada, M. Sixt, Mechanisms of 3D cell migration. Nat. Rev. Mol. Cell Biol. 20, 738–752 (2019).
- J. Schwarz, V. Bierbaum, K. Vaahtomeri, R. Hauschild, M. Brown, I. de Vries, A. Leithner, A. Reversat, J. Merrin, T. Tarrant, T. Bollenbach, M. Sixt, Dendritic cells interpret haptotactic chemokine gradients in a manner governed by signal-to-noise ratio and dependent on GRK6. Curr. Biol. 27, 1314–1325 (2017).
- M. Sarris, M. Sixt, Navigating in tissue mazes: Chemoattractant interpretation in complex environments. Curr. Opin. Cell Biol. 36, 93–102 (2015).
- 43. D. E. Clapham, E. J. Neer, G protein βy subunits. *Annu. Rev. Pharmacol. Toxicol.* **37**, 167–203 (1997).
- D. Kankanamge, M. Tennakoon, A. Karunarathne, N. Gautam, G protein gamma subunit, a hidden master regulator of GPCR signaling. J. Biol. Chem. 298, 102618 (2022).
- D. Vorselen, Y. Wang, M. M. de Jesus, P. K. Shah, M. J. Footer, M. Huse, W. Cai, J. A. Theriot, Microparticle traction force microscopy reveals subcellular force exertion patterns in immune cell-target interactions. *Nat. Commun.* 11, 20 (2020).
- D. Vorselen, S. R. Barger, Y. Wang, W. Cai, J. A. Theriot, N. C. Gauthier, M. Krendel, Phagocytic 'teeth' and myosin-II 'jaw' power target constriction during phagocytosis. eLife 10, e68627 (2021).
- N. Araki, M. T. Johnson, J. A. Swanson, A role for phosphoinositide 3-kinase in the completion of macropinocytosis and phagocytosis by macrophages. J. Cell Biol. 135, 1249–1260 (1996).
- M. Bohdanowicz, D. Schlam, M. Hermansson, D. Rizzuti, G. D. Fairn, T. Ueyama, P. Somerharju, G. Du, S. Grinstein, Phosphatidic acid is required for the constitutive ruffling and macropinocytosis of phagocytes. *Mol. Biol. Cell* 24, 1700–1712 (2013).
- A. K. Mishra, M. Rodriguez, A. Y. Torres, M. Smith, A. Rodriguez, A. Bond, M. A. Morrissey,
 D. J. Montell, Hyperactive Rac stimulates cannibalism of living target cells and enhances
 CAR-M-mediated cancer cell killing. *Proc. Natl. Acad. Sci. U.S.A.* 120, e2310221120 (2023).
- G. Rovera, D. Santoli, C. Damsky, Human promyelocytic leukemia cells in culture differentiate into macrophage-like cells when treated with a phorbol diester. *Proc. Natl. Acad. Sci. U.S.A.* 76, 2779–2783 (1979).
- Z. Liu, P. A. Roche, Macropinocytosis in phagocytes: Regulation of MHC class-II-restricted antigen presentation in dendritic cells. Front. Physiol. 6, 1 (2015).
- 52. M. P. Chao, I. L. Weissman, R. Majeti, The CD47–SIRPα pathway in cancer immune evasion and potential therapeutic implications. *Curr. Opin. Immunol.* **24**, 225–232 (2012).
- M. E. W. Logtenberg, F. A. Scheeren, T. N. Schumacher, The CD47-SIRPα immune checkpoint. *Immunity* 52, 742–752 (2020).
- S. B. Willingham, J. P. Volkmer, A. J. Gentles, D. Sahoo, P. Dalerba, S. S. Mitra, J. Wang, H. Contreras-Trujillo, R. Martin, J. D. Cohen, P. Lovelace, F. A. Scheeren, M. P. Chao, K. Weiskopf, C. Tang, A. K. Volkmer, T. J. Naik, T. A. Storm, A. R. Mosley, B. Edris, S. M. Schmid, C. K. Sun, M. S. Chua, O. Murillo, P. Rajendran, A. C. Cha, R. K. Chin, D. Kim, M. Adorno, T. Raveh, D. Tseng, S. Jaiswal, P. Ø. Enger, G. K. Steinberg, G. Li, S. K. So, R. Majeti, G. R. Harsh, M. van de Rijn, N. N. H. Teng, J. B. Sunwoo, A. A. Alizadeh, M. F. Clarke, I. L. Weissman, The CD47-signal regulatory protein alpha (SIRPa) interaction is a therapeutic target for human solid tumors. *Proc. Natl. Acad. Sci. U.S.A.* 109, 6662–6667 (2012).
- A. R. Jalil, B. H. Hayes, J. C. Andrechak, Y. Xia, D. M. Chenoweth, D. E. Discher, Multivalent, soluble nano-self peptides increase phagocytosis of antibody-opsonized targets while suppressing "self" signaling. ACS Nano 14, 15083–15093 (2020).
- P. L. Rodriguez, T. Harada, D. A. Christian, D. A. Pantano, R. K. Tsai, D. E. Discher, Minimal "self" peptides that inhibit phagocytic clearance and enhance delivery of nanoparticles. Science 339, 971–975 (2013).

- Y. Kitai, M. Ishiura, K. Saitoh, N. Matsumoto, K. Owashi, S. Yamada, R. Muromoto, J. I. Kashiwakura, K. Oritani, T. Matsuda, CD47 promotes T-cell lymphoma metastasis by up-regulating AKAP13-mediated RhoA activation. *Int. Immunol.* 33, 273–280 (2021).
- S. Nagata, K. Segawa, Sensing and clearance of apoptotic cells. Curr. Opin. Immunol. 68, 1–8 (2021).
- D. Cox, C. C. Tseng, G. Bjekic, S. Greenberg, A requirement for phosphatidylinositol 3-kinase in pseudopod extension. *J. Biol. Chem.* 274, 1240–1247 (1999).
- D. Schlam, R. D. Bagshaw, S. A. Freeman, R. F. Collins, T. Pawson, G. D. Fairn, S. Grinstein, Phosphoinositide 3-kinase enables phagocytosis of large particles by terminating actin assembly through Rac/Cdc42 GTPase-activating proteins. *Nat. Commun.* 6, 8623 (2015).
- A. T. Ritter, G. Shtengel, C. S. Xu, A. Weigel, D. P. Hoffman, M. Freeman, N. Iyer, N. Alivodej,
 D. Ackerman, I. Voskoboinik, J. Trapani, H. F. Hess, I. Mellman, ESCRT-mediated membrane repair protects tumor-derived cells against T cell attack. Science 376, 377–382 (2022).
- G. Wang, X. Luo, R. Gu, S. Yang, Y. Qu, S. Zhai, Q. Zhao, K. Li, S. Zhang, PyMIC: A deep learning toolkit for annotation-efficient medical image segmentation. *Comput. Methods Programs Biomed.* 231, 107398 (2023).
- T. A. Masters, B. Pontes, V. Viasnoff, Y. Li, N. C. Gauthier, Plasma membrane tension orchestrates membrane trafficking, cytoskeletal remodeling, and biochemical signaling during phagocytosis. *Proc. Natl. Acad. Sci. U.S.A.* 110, 11875–11880 (2013).
- D. T. Kovari, W. Wei, P. Chang, J. S. Toro, R. F. Beach, D. Chambers, K. Porter, D. Koo,
 J. E. Curtis, Frustrated phagocytic spreading of J774A-1 macrophages ends in myosin II-dependent contraction. *Biophys. J.* 111, 2698–2710 (2016).
- J. Dai, M. P. Sheetz, Mechanical properties of neuronal growth cone membranes studied by tether formation with laser optical tweezers. *Biophys. J.* 68, 988–996 (1995).
- L. Bo, R. E. Waugh, Determination of bilayer membrane bending stiffness by tether formation from giant, thin-walled vesicles. *Biophys. J.* 55, 509–517 (1989).
- V. Heinrich, R. E. Waugh, A piconewton force transducer and its application to measurement of the bending stiffness of phospholipid membranes. *Ann. Biomed. Eng.* 24, 595–605 (1996).
- D. Raucher, M. P. Sheetz, Characteristics of a membrane reservoir buffering membrane tension. *Biophys. J.* 77, 1992–2002 (1999).
- E. N. Glaros, W. S. Kim, B. J. Wu, C. Suarna, C. M. Quinn, K. A. Rye, R. Stocker, W. Jessup,
 B. Garner, Inhibition of atherosclerosis by the serine palmitoyl transferase inhibitor myriocin is associated with reduced plasma glycosphingolipid concentration. *Biochem. Pharmacol.* 73, 1340–1346 (2007).
- J. M. Wadsworth, D. J. Clarke, S. A. McMahon, J. P. Lowther, A. E. Beattie, P. R. R. Langridge-Smith, H. B. Broughton, T. M. Dunn, J. H. Naismith, D. J. Campopiano, The chemical basis of serine palmitoyltransferase inhibition by myriocin. *J. Am. Chem. Soc.* 135, 14276–14285 (2013).
- C. J. Greene, J. A. Nguyen, S. M. Cheung, C. R. Arnold, D. R. Balce, Y. T. Wang, A. Soderholm, N. McKenna, D. Aggarwal, R. I. Campden, B. W. Ewanchuk, H. W. Virgin, R. M. Yates, Macrophages disseminate pathogen associated molecular patterns through the direct extracellular release of the soluble content of their phagolysosomes. *Nat. Commun.* 13, 3072 (2022).
- T. E. Khoyratty, Z. Ai, I. Ballesteros, H. L. Eames, S. Mathie, S. Martin-Salamanca, L. Wang, A. Hemmings, N. Willemsen, V. von Werz, A. Zehrer, B. Walzog, E. van Grinsven, A. Hidalgo, I. A. Udalova, Distinct transcription factor networks control neutrophil-driven inflammation. *Nat. Immunol.* 22, 1093–1106 (2021).
- H. Zhang, M. P. Reilly, Human induced pluripotent stem cell-derived macrophages for unraveling human macrophage biology. *Arterioscler. Thromb. Vasc. Biol.* 37, 2000–2006 (2017).
- A. Vaughan-Jackson, S. Stodolak, K. H. Ebrahimi, C. Browne, P. K. Reardon, E. Pires, J. Gilbert-Jaramillo, S. A. Cowley, W. S. James, Differentiation of human induced pluripotent stem cells to authentic macrophages using a defined, serum-free, open-source medium. Stem Cell Rep. 16, 3093 (2021).
- C. Alsinet, M. N. Primo, V. Lorenzi, E. Bello, I. Kelava, C. P. Jones, R. Vilarrasa-Blasi, C. Sancho-Serra, A. J. Knights, J. E. Park, B. S. Wyspianska, G. Trynka, D. F. Tough, A. Bassett, D. J. Gaffney, D. Alvarez-Errico, R. Vento-Tormo, Robust temporal map of human in vitro myelopoiesis using single-cell genomics. *Nat. Commun.* 13, 2885 (2022).
- M. A. Giese, L. E. Hind, A. Huttenlocher, Neutrophil plasticity in the tumor microenvironment. *Blood* 133, 2159–2167 (2019).
- Y. Guo, S. Kasahara, A. Jhingran, N. L. Tosini, B. Zhai, M. A. Aufiero, K. A. M. Mills, M. Gjonbalaj, V. Espinosa, A. Rivera, A. D. Luster, T. M. Hohl, During aspergillus infection, monocyte-derived DCs, neutrophils, and plasmacytoid DCs enhance innate immune defense through CXCR3-dependent crosstalk. *Cell Host Microbe* 28, 104–116. e4 (2020).
- M. M. Mircescu, L. Lipuma, N. van Rooijen, E. G. Pamer, T. M. Hohl, Essential role for neutrophils but not alveolar macrophages at early time points following *Aspergillus fumigatus* infection. *J. Infect. Dis.* 200, 647–656 (2009).

SCIENCE IMMUNOLOGY | RESEARCH ARTICLE

- V. Espinosa, O. Dutta, L. J. Heung, K. Wang, Y. J. Chang, P. Soteropoulos, T. M. Hohl, M. C. Siracusa, A. Rivera, Cutting edge: Neutrophils license the maturation of monocytes into effective antifungal effectors. *J. Immunol.* 209, 1827–1831 (2022).
- M. Monod, S. Paris, J. Sarfati, K. Jaton-Ogay, P. Ave, J. P. Latge, Virulence of alkaline protease-deficient mutants of Aspergillus fumigatus. FEMS Microbiol. Lett. 106, 39–46 (1993).
- W. Wei, L. Zhang, W. Xin, Y. Pan, L. Tatenhorst, Z. Hao, S. T. Gerner, S. Huber, M. Juenemann, M. Butz, H. B. Huttner, M. Bahr, D. Fitzner, F. Jia, T. R. Doeppner, TREM2 regulates microglial lipid droplet formation and represses post-ischemic brain injury. *Biomed. Pharmacother.* 170, 115962 (2024).
- X. W. Pang, Y. H. Chu, L. Q. Zhou, M. Chen, Y. F. You, Y. Tang, S. Yang, H. Zhang, J. Xiao, G. Deng, W. Wang, K. Shang, C. Qin, D. S. Tian, Trem2 deficiency attenuates microglial phagocytosis and autophagic-lysosomal activation in white matter hypoperfusion. J. Neurochem. 167, 489–504 (2023).
- A. Castoldi, D. E. Sanin, N. van Teijlingen Bakker, C. F. Aguiar, L. de Brito Monteiro, N. Rana, K. M. Grzes, A. M. Kabat, J. Curtis, A. M. Cameron, G. Caputa, T. Antonio de Souza, F. O. Souto, J. M. Buescher, J. Edwards-Hicks, E. L. Pearce, E. J. Pearce, N. O. Saraiva Camara, Metabolic and functional remodeling of colonic macrophages in response to high-fat diet-induced obesity. *IScience* 26, 107719 (2023).
- T. C. Walther, R. V. Farese Jr., Lipid droplets and cellular lipid metabolism. Annu. Rev. Biochem. 81, 687–714 (2012).
- 85. R. V. Farese Jr., T. C. Walther, Glycerolipid synthesis and lipid droplet formation in the endoplasmic reticulum. *Cold Spring Harb. Perspect. Biol.* **15**, a041246 (2023).
- E. Jarc, T. Petan, Lipid droplets and the management of cellular stress. Yale J. Biol. Med. 92, 435–452 (2019).
- J. A. Olzmann, P. Carvalho, Dynamics and functions of lipid droplets. Nat. Rev. Mol. Cell Biol. 20, 137–155 (2019).
- C. Hetz, K. Zhang, R. J. Kaufman, Mechanisms, regulation and functions of the unfolded protein response. Nat. Rev. Mol. Cell Biol. 21, 421–438 (2020).
- P. Lassuthova, D. Safka Brozkova, J. Neupauerova, M. Krutova, R. Mazanec, P. Seeman, Confirmation of the GNB4 gene as causal for Charcot-Marie-Tooth disease by a novel de novo mutation in a Czech patient. *Neuromuscul. Disord.* 27, 57–60 (2017).
- B. W. Soong, Y. H. Huang, P. C. Tsai, C. C. Huang, H. C. Pan, Y. C. Lu, H. J. Chien, T. T. Liu, M. H. Chang, K. P. Lin, P. H. Tu, L. S. Kao, Y. C. Lee, Exome sequencing identifies GNB4 mutations as a cause of dominant intermediate Charcot-Marie-Tooth disease. *Am. J. Hum. Genet.* 92, 422–430 (2013).
- 91. Y. H. Hsu, K. P. Lin, Y. C. Guo, Y. S. Tsai, Y. C. Liao, Y. C. Lee, Mutation spectrum of Charcot-Marie-Tooth disease among the Han Chinese in Taiwan. *Ann. Clin. Transl. Neurol.* **6**, 1090–1101 (2019).
- H. M. Kwon, H. S. Kim, S. B. Kim, J. H. Park, D. E. Nam, A. J. Lee, S. H. Nam, S. Hwang, K. W. Chung, B.-O. Choi, Clinical and neuroimaging features in Charcot-Marie-Tooth patients with GNB4 mutations. Life 11. 494 (2021).
- R. E. Zigmond, F. D. Echevarria, Macrophage biology in the peripheral nervous system after injury. Prog. Neurobiol. 173, 102–121 (2019).
- J. Kolter, K. Kierdorf, P. Henneke, Origin and differentiation of nerve-associated macrophages. J. Immunol. 204, 271–279 (2020).
- D. Klein, A. Patzko, D. Schreiber, A. van Hauwermeiren, M. Baier, J. Groh, B. L. West, R. Martini, Targeting the colony stimulating factor 1 receptor alleviates two forms of Charcot-Marie-Tooth disease in mice. *Brain* 138, 3193–3205 (2015).
- D. Klein, J. Groh, A. Weishaupt, R. Martini, Endogenous antibodies contribute to macrophage-mediated demyelination in a mouse model for CMT1B. J. Neuroinflammation 12, 49 (2015).
- S. Carenini, M. Maurer, A. Werner, H. Blazyca, K. V. Toyka, C. D. Schmid, G. Raivich, R. Martini, The role of macrophages in demyelinating peripheral nervous system of mice heterozygously deficient in po. J. Cell Biol. 152, 301–308 (2001).
- C. Sloas, S. Gill, M. Klichinsky, Engineered CAR-macrophages as adoptive immunotherapies for solid tumors. Front. Immunol. 12, 783305 (2021).
- J. Folch, M. Lees, G. H. Sloane Stanley, A simple method for the isolation and purification of total lipides from animal tissues. J. Biol. Chem. 226, 497–509 (1957).
- J. P. Koelmel, X. Li, S. M. Stow, M. J. Sartain, A. Murali, R. Kemperman, H. Tsugawa, M. Takahashi, V. Vasiliou, J. A. Bowden, R. A. Yost, T. J. Garrett, N. Kitagawa, Lipid annotator: Towards accurate annotation in non-targeted liquid chromatography

- high-resolution tandem mass spectrometry (LC-HRMS/MS) lipidomics using a rapid and user-friendly software. *Metabolites* **10**, 101 (2020).
- 101. K. J. Adams, B. Pratt, N. Bose, L. G. Dubois, L. St John-Williams, K. M. Perrott, K. Ky, P. Kapahi, V. Sharma, M. J. MacCoss, M. A. Moseley, C. A. Colton, B. X. MacLean, B. Schilling, J. W. Thompson, C., Skyline for small molecules: A unifying software package for quantitative metabolomics. J. Proteome Res. 19, 1447–1458 (2020).
- S. Murao, M. A. Gemmell, M. F. Callaham, N. L. Anderson, E. Huberman, Control of macrophage cell differentiation in human promyelocytic HL-60 leukemia cells by 1,25-dihydroxyvitamin D3 and phorbol-12-myristate-13-acetate. *Cancer Res.* 43, 4989–4996 (1983).
- P. J. Punt, R. P. Oliver, M. A. Dingemanse, P. H. Pouwels, C. A. van den Hondel, Transformation of Aspergillus based on the hygromycin B resistance marker from Escherichia coli. Gene 56, 117–124 (1987).
- L. Mikkelsen, S. Sarrocco, M. Lubeck, D. F. Jensen, Expression of the red fluorescent protein DsRed-Express in filamentous ascomycete fungi. FEMS Microbiol. Lett. 223, 135–139 (2003).
- G. G. Wang, K. R. Calvo, M. P. Pasillas, D. B. Sykes, H. Hacker, M. P. Kamps, Quantitative production of macrophages or neutrophils ex vivo using conditional Hoxb8. *Nat. Methods* 3, 287–293 (2006).
- J. D. Miller, Y. M. Ganat, S. Kishinevsky, R. L. Bowman, B. Liu, E. Y. Tu, P. K. Mandal, E. Vera, J. W. Shim, S. Kriks, T. Taldone, N. Fusaki, M. J. Tomishima, D. Krainc, T. A. Milner, D. J. Rossi, L. Studer, Human iPSC-based modeling of late-onset disease via progerin-induced aging. Cell Stem Cell 13, 691–705 (2013).
- N. Lachmann, M. Ackermann, E. Frenzel, S. Liebhaber, S. Brennig, C. Happle, D. Hoffmann, O. Klimenkova, D. Luttge, T. Buchegger, M. P. Kuhnel, A. Schambach, S. Janciauskiene, C. Figueiredo, G. Hansen, J. Skokowa, T. Moritz, Large-scale hematopoietic differentiation of human induced pluripotent stem cells provides granulocytes or macrophages for cell replacement therapies. Stem Cell Reports 4, 282–296 (2015).
- E. J. Quann, E. Merino, T. Furuta, M. Huse, Localized diacylglycerol drives the polarization of the microtubule-organizing center in T cells. *Nat. Immunol.* 10, 627–635 (2009)

Acknowledgments: We thank the Molecular Cytology Core Facility, the Cell Metabolism Core Facility, the Flow Cytometry Core Facility, and the Integrated Genomics Operation at MSKCC for technical support; the New York Structural Biology Center for assistance with FIB-SEM; and members of the laboratories of M.H., O.D.W., and J.G.C. for advice, Funding: This work was supported, in part, by the NIH (R01-Al087644 to M.H., R35-GM118167 to O.D.W., R01-Al45073 to J.G.C., R25-AI40472 to J.R.C., R21AI50244 to L.C.K., R01-NS115715 to F.G., R01-AI130345 to F.G., and P30-CA008748 to MSKCC), the NSF (2019598 and 1548297 to O.D.W.), the Donald B. and Catherine C. Marron Cancer Metabolism Center (J.R.C.), the Schmidt Science Fellows Program (B.Y.W.), the Cancer Research Institute (B.Y.W.), and the MSKCC Basic Research Postdoc Innovation Award (B.Y.W.), Author contributions: B.Y.W., J.G.C., O.D.W., and M.H. conceived of the project, analyzed the data, and wrote the manuscript, B.Y.W., A.H.S., A.M.Y., C.J., T.L., M.T., M.S., A.S., A.-L.L.S., M.G., Y.Y.W., J.C., T.Z., and H.A.P. performed experiments or analysis for the manuscript. F.G., L.C.K., J.S.A.P., and T.H. provided reagents and helpful expertise. Competing interests: B.Y.W., O.D.W., J.G.C., and M.H. have applied for a patent on the discovery that knockout or null mutations in Gβ4 leads to increased phagocytosis in professional phagocytic cells (PCT/US2024/019787), J.G.C. is a member of the Scientific Advisory Board of Be Biopharma and consults for Lycia Therapeutics and Dren Bio Inc. All other authors declare that they have no competing interests. Data and materials availability: RNA sequencing data have been deposited with the BioSample (SAMN41132906), BioProject (PRJNA1106430), and SRA (PRJNA1106430) repositories. Custom MATLAB code may be found at GitHub (https:// github.com/benjaminywiner/) or Zenodo (10.5281/zenodo.11193030, 10.5281/ zenodo.11193125, and 10.5281/zenodo.11193130). Tabulated data underlying the figures are provided in data file S2. All other data needed to support the conclusions of the paper are present in the paper itself or the Supplementary Materials. $\mathsf{Gnb4}^{-\prime-}$ mice, hiPSC cell lines, and all other reagents are available via material transfer agreement. Requests for reagents should be addressed to B.Y.W. (winerb@mskcc.org) or M.H. (husem@mskcc.org).

Submitted 6 October 2023 Accepted 15 May 2024 Published 7 June 2024 10.1126/sciimmunol.adl2388